https://doi.org/10.5194/egusphere-2026-27
Preprint. Discussion started: 20 January 2026

What matters when? Temporal development of drivers and sources of nitrous oxide emissions in winter wheat

Fabio Turco[1], Iris Feigenwinter[1], Lorenz Allemann[1], Lukas Hörtnagl[1], Frank Liebisch[2], Nina Buchmann[1]

[1]Institute of Agricultural Sciences, ETH Zurich, Zurich, Switzerland
[2]Agroscope, Department of Agroecology and Environment, Zurich, Switzerland

Correspondence to: Fabio Turco (Fabio.turco@usys.ethz.ch)

Abstract. Agriculture is the largest anthropogenic source of nitrous oxide (N_2O), primarily due to nitrogen (N) fertilization. Understanding how the influence of key drivers and the relative contribution of source processes change throughout the cropping season is crucial for developing effective strategies to mitigate N_2O emissions. In this study, we combined high-resolution eddy covariance flux measurements and stable isotope analyses over one winter wheat cropping season and the subsequent summer cover crop season. Two phases, crop establishment and early spring, were identified as critical periods for N_2O emissions, characterized by a mismatch between N supply and plant demand, resulting in surplus soil mineral N and elevated N_2O fluxes under favorable environmental conditions. Gross primary productivity (GPP), used as a proxy for crop N uptake, suppressed N_2O emissions, especially under high soil moisture, highlighting the importance of active vegetation in mitigating emissions. Source partitioning, based on stable isotopes, revealed denitrification as the dominant process of N_2O production, driven by poor soil drainage and high soil moisture. Over the nine-month winter wheat season, the Tier 1 N_2O emission factor was 1.8%, with cumulative emissions of 5.5 kg N_2O-N ha^{-1}, offsetting 70% of the net CO_2 uptake. Our findings emphasize the need to better synchronize N supply with crop demand and to adopt agronomic practices that promote rapid crop establishment to mitigate N_2O emissions in cropping systems.

Keywords: arable land; nitrous oxide; winter wheat; cover crop; eddy covariance; stable isotopes; drivers

1 Introduction

Nitrogen (N) is an essential nutrient for crop production, and the use of N fertilizers plays a central role in ensuring global food security (Erisman et al., 2008; Liang, 2022). However, a large part of the applied N is lost to the environment due to misalignment between the application (amount and timing) and crop demand (Ladha et al., 2005). Globally, only about 47% of total fertilizer N input is taken up by crops, with the remainder lost primarily through nitrate (NO_3^-) leaching and ammonia (NH_3) volatilization, contributing to water and air pollution (Lassaletta et al., 2014). Approximately 1% of the applied N (IPCC, 2019) is emitted as nitrous oxide (N_2O), a potent greenhouse gas (GHG) with a 100-year global warming potential (GWP_{100}) of 273 times that of CO_2 (Forster et al., 2021), and the dominant ozone-depleting substance of the current century

https://doi.org/10.5194/egusphere-2026-27
Preprint. Discussion started: 20 January 2026

(Portmann et al., 2012; Ravishankara et al., 2009). Together with carbon dioxide (CO_2) and methane (CH_4), N_2O represents one of the three major greenhouse gases contributing to anthropogenic climate forcing, with agricultural soils being a significant source of all three (Nabuurs et al., 2022). Despite accounting for a relatively minor fraction of N losses, the climate impact of N_2O makes its mitigation a key priority in sustainable agricultural management. Direct N_2O emissions from agricultural N additions represent the largest source of anthropogenic N_2O emissions, contributing 56% of global emissions over the past decade (Tian et al., 2024), with more than half (55%) originating from soils following fertilizer application. The remaining fraction is attributed to manure excreted on pastures and manure management (Epper et al., 2025; Tian et al., 2024). In Switzerland, N_2O emissions account for approximately 30% of total agricultural GHG emissions (FOEN, 2025). At both EU and Swiss levels, policies have been introduced to reduce N losses from agriculture and mitigate associated environmental impacts, such as the EU Nitrates Directive (European Commission, 1991) and Switzerland's Water Protection Ordinance (Swiss Federal Council, 1998). However, despite the well-documented climate effects of N_2O, binding measures specifically targeting N_2O mitigation are still lacking (Epper et al., 2025). This regulatory gap hinders the development and implementation of effective mitigation strategies, leaving a major source of agricultural greenhouse gas emissions largely unaddressed.

N_2O in soils is primarily produced through microbial nitrification and denitrification, processes that are regulated by a complex interplay of dynamic factors, including the availability of N substrates (i.e., NH_4^+ and NO_3^-), soil moisture, temperature, pH, and availability of labile carbon (Butterbach-Bahl et al., 2013; Davidson, 1991; Rummel et al., 2025; Smith, 2017). Agronomic operations such as fertilization and tillage increase N availability and stimulate microbial N_2O production (Chatskikh and Olesen, 2007; Shcherbak et al., 2014). Recent studies also highlight the role of actively growing vegetation as a dynamic N sink that competes with microbes for N substrates, thereby reducing their availability for N_2O production and mitigating N_2O emissions (Feigenwinter et al., 2023; Maier et al., 2022; Timilsina et al., 2024). Accordingly, the N surplus, defined as the difference between total N inputs and outputs, correlates positively with N_2O emissions (Tallec et al., 2022; Van Groenigen et al., 2010). However, the spatio-temporal heterogeneity of environmental and management-related drivers, along with the high temporal variability of N_2O fluxes, pose major challenges for identifying key drivers of N_2O losses throughout the cropping season. Each phase, from field preparation to post-harvest, is controlled by distinct processes and their interactions (Smith et al., 1998). While many studies have explored the general relationships between individual drivers and N_2O emissions, to our knowledge, no study has systematically investigated how the relative importance of these drivers changes over the course of a cropping season. Therefore, our understanding of these temporal dynamics is still scarce, limiting the development of mitigation strategies because these may only be effective when aligned with the dominant emission controls at specific stages of the cropping season.

In addition to N_2O, croplands exchange substantial amounts of CO_2 and CH_4 with the atmosphere, which together determine their net greenhouse gas (GHG) budget (Carlson et al., 2017; Ciais et al., 2010; Schulze et al., 2009). CO_2 fluxes reflect the difference between photosynthetic carbon uptake and ecosystem respiration, whereas CH_4 fluxes from agricultural soils result from concurrent microbial production (i.e., methanogenesis) and oxidation (i.e., methanotrophy) (Le Mer and Roger,

https://doi.org/10.5194/egusphere-2026-27
Preprint. Discussion started: 20 January 2026

2001). Quantifying these fluxes alongside N_2O is crucial for an integrated assessment of the cropland GHG budget and its response to environmental and management drivers.

To improve our understanding of the temporal dynamics of N_2O emissions and their contribution to the full GHG budget, continuous and spatially integrated measurements of N_2O fluxes are essential. Micrometeorological techniques such as eddy covariance (EC) enable continuous, high-frequency observations of N_2O fluxes, spatially integrating over entire fields (Feigenwinter et al., 2023; Lognoul et al., 2019; Maier et al., 2022, 2025). When EC-based N_2O flux measurements are combined with concurrent observations of key environmental and management-related drivers, they can provide valuable insights into the temporal dynamics of N_2O emissions and their controls throughout the cropping season. Building on high-resolution data provided by EC systems, machine learning (ML) algorithms offer powerful tools to model N_2O emissions (Gnisia et al., 2025; Goodrich et al., 2021; Hamrani et al., 2020). These ML models can capture non-linear relationships and complex interactions among environmental and management-related drivers and often outperform traditional statistical approaches in predictive accuracy (Philibert et al., 2013; Saha et al., 2021). Furthermore, model explanation techniques such as SHapley Additive exPlanations (SHAP; Lundberg and Lee, 2017) enhance the interpretability of ML models by quantifying the contribution of individual drivers, offering insights into the temporal evolution of driver importance (Krebs et al., 2025; Scapucci et al., 2024, 2025).

While ML models can identify which environmental and management variables most influence N_2O fluxes, they do not reveal the underlying microbial production processes. This distinction is important because nitrification and denitrification respond differently to environmental conditions (Butterbach-Bahl et al., 2013; Davidson, 1991) and management (Buchen et al., 2018). Distinguishing between these two sources of N_2O is essential for developing targeted mitigation strategies and improving the accuracy of process-based biogeochemical models (Del Grosso et al., 2020). Stable isotope analysis, particularly of the intramolecular distribution of ^{15}N (i.e., site preference, SP), offers a robust approach to identify the relative contributions of nitrification and denitrification to N_2O production (Toyoda and Yoshida, 1999). These microbial processes generate N_2O with distinct isotopic signatures due to differences in enzymatic mechanisms and substrate pools. Because SP is largely independent of the isotopic composition of precursor substrates, it enables robust source partitioning under field conditions (Decock and Six, 2013). Combined with N and O stable isotope ratios ($\delta^{15}N$ and $\delta^{18}O$, respectively), SP allows tracing the temporal development of N_2O-producing processes (Verhoeven et al., 2019; Yu et al., 2020).

The present study integrates continuous EC measurements, ML-based driver analysis, and stable isotope techniques to provide a comprehensive assessment of N_2O emissions over a winter wheat cropping season and the following short summer cover crop at a study site with a temperate climate in Europe. Specifically, we aimed to (i) quantify N_2O, CO_2, and CH_4 fluxes and resulting GHG budgets throughout a winter wheat cropping season and the subsequent cover crop season, (ii) determine the temporal development of environmental and management driver contributions to N_2O fluxes, and (iii) identify the contributions of different microbial N_2O-producing processes and their temporal development after a fertilization event.

https://doi.org/10.5194/egusphere-2026-27
Preprint. Discussion started: 20 January 2026

2 Material and methods

2.1 Study site

The study site is a cropland field in Oensingen, canton of Solothurn, Switzerland. The site has a mean annual temperature of 10.1 °C and receives an average of 1151 mm of precipitation per year (2004-2023). CO_2 and water vapor (H_2O) fluxes have been continuously measured at the site by a EC station (CH-Oe2, part of FLUXNET; 47°10′41.5″ N, 7°39′54.4″ E; 465 m a.s.l.) since December 2003 (Emmel et al., 2018). The field where the station is positioned has an area of 1.55 ha, and the soil is an Eutric-Stagnic Cambisol with a silty clay soil texture. In the top 25 cm depth, the soil consists of 43% clay, 47% silt, and 10% sand, with 2.8% organic matter (Alaoui and Goetz, 2008). The field is managed according to an integrated farming label (IP Swiss), and follows the Proof of Ecological Performance (PEP; Swiss Federal Council, 2025). PEP sets baseline requirements for receiving direct payments, including rules for crop rotation, farm-based fertilizer use, and measures to protect soil and biodiversity. Over the past 20 years, the crop rotation included various annual crops, with winter wheat as primary crop. A temporary grassland (grass-clover mixture; STEFFEN 3003M, Samen STEFFEN AG) was established in 2020 and managed until its final cut in late September 2022, followed by herbicide application (Glyphosate) and direct-seeding of winter wheat. This study was conducted over one year, from September 2022 to October 2023, covering the last month of the temporary grassland, the full winter wheat growing season, and the subsequent cover crop season, a mixture of legumes, grasses, and forbs (Terra-FIT Quattro, Samen STEFFEN AG). Winter wheat (Montalbano, bred by Agroscope and DSP) was sown on October 6, 2022, and harvested on July 15, 2023, with 5.03 t ha^{-1} grain yield (dry matter). The winter wheat received three applications of mineral and organic (dairy slurry) fertilizers between late tillering and early stem elongation, summing up to 138 kg N ha^{-1} (Table 1). After the harvest, the straw was removed from the field, and the soil was cultivated for the subsequent sowing of the summer cover crop. The cover crop was mulched in late September 2023, before the soil was cultivated again to prepare for the sowing of winter barley in early October 2023.

Table 1. Main management activities conducted during the 2022-2023 measurement period at the cropland in Oensingen. Positive values for nitrogen (N) in/output (kg ha^{-1}) indicate inputs to the field, whereas negative values represent N exports. For organic fertilization, total N is reported, with the NH_4^+-N fraction shown in parentheses. Due to a sampling issue in 2023, slurry composition was estimated based on laboratory analysis of a 2024 sample from the same farm. Harvest-related N exports are reported as mean ± 1 standard deviation. Details on commercial products and additional management practices are provided in Table A1.

Crop	Management activity	Date	N in/output
Grass-clover	Harvest	20 September 2022	- 40 ± 7
	Herbicide application	3 October 2022	
Winter wheat	Sowing (direct seeding)	6 October 2022	+5.2
	Ammonium nitrate application	27 February 2023	+68
	Slurry application (dairy)	28 February 2023	+43 (+18)
	Ammonium nitrate application	6 April 2023	+27
	Harvest (grain and straw)	15 July 2023	-162 ± 53

https://doi.org/10.5194/egusphere-2026-27
Preprint. Discussion started: 20 January 2026

Bare soil	Soil cultivation	17 July 2023	
Cover crop	Sowing	27 July 2023	+1.4
	Mulching	25 September 2023	
Bare soil	Soil cultivation	27 September 2023	

2.2 Eddy covariance flux measurements

2.2.1 Setup

The EC setup, situated at the center of the field, consisted of an ultrasonic anemometer (R3-50, Gill Instruments Ltd., Lymington, UK) that measured wind speed, and a laser spectrometer that measured N_2O and CH_4 concentrations at 10 Hz (GLA351-N2OM1, Los Gatos Research, Mountain View, CA, USA), as well as an enclosed infrared gas analyzer (IRGA) that measured CO_2 and H_2O concentrations at 20 Hz (LI-7200, LI-COR Biosciences, Lincoln NE, USA). The laser spectrometer was connected to an external pump (EV-A06, Ebara Technologies, Sacramento, CA, USA) and both were placed in temperature-controlled boxes. A 7 m long, 7.5 mm diameter unheated polyethylene/aluminum composite tube (EATON Synflex 1300, Dublin, Ireland) was used to draw air to the laser spectrometer. The measurement height of the sonic anemometer was 2.17 m above ground, and the inlets of the laser spectrometer and the IRGA were mounted approximately 0.2 m below the sonic anemometer. While CO_2 and H_2O fluxes have been measured continuously since 2003, N_2O and CH_4 flux measurements were conducted during selected periods between 2018 and 2021 (Maier et al., 2025), followed by continuous measurements from 30 August 2022 to 5 October 2023 in the present study.

2.2.2 Flux processing

Half-hourly fluxes of CO_2, H_2O (i.e., as latent heat flux (LE)), as well as N_2O and CH_4 fluxes were calculated using the EddyPro software (version 7.0.9, LI-COR Environmental, Lincoln NE, USA) following established EC flux community protocols (Aubinet et al., 2012; Nemitz et al., 2018; Pastorello et al., 2020; Sabbatini et al., 2018). Raw high-frequency data underwent de-spiking and screening, in line with Vickers and Mahrt (1997), and wind components were aligned using a 2D rotation method (Wilczak et al., 2001). The time lag between the vertical wind component and scalar concentration of N_2O and CH_4 was set to a constant value, corresponding to the most frequently occurring lag (1.40 s for N_2O and 1.50 s for CH_4) identified through covariance maximization within a broad window (0-5 s) over the entire measurement period. In contrast, time lags for CO_2 and LE were determined dynamically through covariance maximization within narrow windows, based on prior lag distributions identified using a broader window. When no clear covariance peak was detected within the defined window, a default lag was applied (1.30 s for CO_2, 1.45 s for H_2O), corresponding to the most frequently identified lag in the earlier analysis. Spectral corrections addressed high-pass (Moncrieff et al., 2005) and low-pass filtering effects (Fratini et al., 2012). A correction for instrument separation was applied (Horst and Lenschow, 2009). The flux footprint model by Kljun et al. (2015) estimated the upwind area contributing to the measured flux.

https://doi.org/10.5194/egusphere-2026-27
Preprint. Discussion started: 20 January 2026

2.2.3 Quality assessment and de-spiking

Data quality was assessed using a composite flag (QC0 = best quality, QC1 = medium quality, QC2 = bad quality), calculated with the Python library *diive* (v0.86.0; Hörtnagl, 2025). The flag included tests for (1) steady-state and integral turbulence characteristics (Mauder and Foken, 2004), (2) spectral correction factor (values with spectral correction factor > 4 were excluded), (3) IRGA signal strength, (4) completeness of the averaging interval (if <97% coverage within 30 min, value was excluded; Sabbatini et al., 2018), and (5) occurrence of spikes and drop-outs in the raw data after the statistical tests by Vickers and Mahrt (1997). Fluxes with the quality flag 2 (QC2) were excluded from further analyses. Storage terms (single point measurement) were added to all measured gas fluxes (Aubinet et al., 2001). CO_2 fluxes are referred to as net ecosystem exchange of CO_2 (NEE) from this point onwards. Absolute limits were applied to remove half-hourly fluxes outside plausible ranges, determined by analyzing typical ranges for highest-quality fluxes (NEE: - 60 to 50 µmol m^{-2} s^{-1}; LE: -50 to 800 W m^{-2}; N_2O: - 3 to 30 nmol m^{-2} s^{-1}; CH_4: - 30 to 80 nmol m^{-2} s^{-1}). Outliers were further removed using two statistical filters: a Hampel filter applied separately for daytime and nighttime periods, and a rolling z-score method. Finally, a friction velocity (u_*) filter (Papale et al., 2006) was applied to NEE, N_2O, and CH_4 fluxes to exclude periods with insufficient turbulence conditions. The threshold was determined using CO_2 fluxes, and a constant u_* threshold of 0.092 m s^{-1} was used for the entire study period. After applying all quality checks, de-spiking, and u_* filtering, data coverage for fluxes over the entire measurement period was 50.8% for NEE, 68.5% for LE, 52.9% for N_2O fluxes, and 33.6% for CH_4 fluxes. Only the highest quality N_2O fluxes (QC0, 34.5% data coverage) were used for the driver analysis. Further details on data quality control procedures and outlier removal methods are available in the project repository (Turco, 2025a). Flux rates are reported as µmol CO_2 m^{-2} s^{-1} for NEE, nmol N_2O m^{-2} s^{-1} for N_2O flux, and nmol CH_4 m^{-2} s^{-1} for CH_4 flux, while cumulative fluxes are reported as g C m^{-2} (NEE, CH_4) or kg N_2O-N ha^{-1} (N_2O).

2.2.4 Gap-filling and NEE partitioning

Gap-filling of N_2O and CH_4 fluxes was performed using the Random Forest (RF) algorithm (Breiman, 2001) as implemented via the *diive* Python library (v. 0.86.0), based on the *scikit-learn* (v1.15) framework. Predictor (i.e., driver) variables were selected based on their demonstrated predictive performance in previous studies (Feigenwinter et al., 2023; Maier et al., 2022), including environmental data (and their lagged variants), management information (expressed as time since event), and timestamp features. Environmental variables comprised soil temperature, precipitation (in absolute terms and time since occurrence), and soil water content.

For NEE and LE, gap-filling was conducted using the Marginal Distribution Sampling (MDS) method (Reichstein et al., 2005), implemented in R via the *REddyProc* package (v. 1.3.2; Wutzler et al., 2018). Input variables for MDS included global radiation, air temperature, and vapor pressure deficit. NEE was subsequently partitioned into gross primary production (GPP) and ecosystem respiration (R_{eco}) using the night-time method (Reichstein et al., 2005), also implemented

https://doi.org/10.5194/egusphere-2026-27
Preprint. Discussion started: 20 January 2026

in *REddyProc* (Wutzler et al., 2018). Additional methodological details and code are available in the project repository (Turco, 2025a).

2.3 Calculating N_2O emission factor and GHG budgets

The N_2O emission factor (EF) for winter wheat was calculated by dividing the cumulative N_2O-N emissions attributable to fertilization (excluding background fluxes) by the total amount of N from synthetic and organic fertilizers. This calculation excluded background fluxes and followed the IPCC Tier 1 approach (IPCC, 2019). The background N_2O flux was calculated as the average of gap-filled fluxes, omitting 30-day post-fertilization periods to remove the short-term fertilization effects. The resulting EF is expressed as the percentage of the applied N that is emitted as N_2O-N.

The GHG budgets for CO_2, N_2O, and CH_4 were calculated separately for the winter wheat and cover crop cropping seasons (282 and 60 days, respectively), covering the period from sowing to harvest, using gap-filled flux datasets (see Sect. 2.2.4 for gap-filling procedure). To express fluxes in terms of CO_2-equivalents, global warming potential (GWP_{100}) values of 273 for N_2O and 27 for CH_4 were applied, in accordance with current estimates (Forster et al., 2021).

2.4 Meteorological and soil variables

The meteorological variables air temperature and relative humidity (CS215, Campbell Scientific Ltd., Logan UT, USA), atmospheric pressure (PAA-33X, Keller AG, Switzerland), short- and longwave radiation (CNR4, Kipp & Zonen, Delft, Netherlands), photosynthetic photon flux density PPFD (BF5, Delta-T Devices, United Kingdom), and precipitation (heated tipping bucket rain gauge, Lambrecht meteo GmbH, Germany) were measured continuously at the EC station. Soil water content and soil temperature were also measured continuously close to the EC station along one soil profile (at 0.05, 0.15, 0.3, and 0.5 m soil depths) using 5TM sensors (Decagon Devices, Inc., Pullman WA, USA). All meteorological measurements were recorded at one-minute time resolution and, after screening for outliers, averaged to 30-minute values (precipitation was summed). Water-filled pore space (WFPS; Eq. 1) was calculated for each soil depth as:

$$WFPS = \frac{SWC}{1-\frac{BD}{PD}} * 100 \quad (1)$$

where SWC is the volumetric soil water content (in $m^3\ m^{-3}$), BD is the bulk density (in $g\ cm^{-3}$), with values of 1.16, 1.40, and 1.33 $g\ cm^{-3}$ for the 0-0.05, 0.15-0.3, and 0.3-0.5 m depth intervals, respectively, obtained from Emmel et al. (2018), and PD is the particle density, assumed to be 2.65 $g\ cm^{-3}$ (Danielson and Sutherland 1986).

2.5 Soil chamber measurements and stable isotope analyses

Five opaque static PVC (polyvinyl chloride) chambers, each with a volume of 17.7 L and a surface area of 0.07 m^2, were deployed at five randomly selected locations within a 12 m radius of the EC station (Fig. 1). The chambers were first deployed on 24 February 2023, before the first fertilization event, and positioned to enclose plants from two adjacent wheat rows. To ensure that regular field management could continue unhindered, the chambers were removed immediately after

https://doi.org/10.5194/egusphere-2026-27
Preprint. Discussion started: 20 January 2026

sampling when management operations were scheduled before the next sampling date and subsequently reinstalled at the same positions for the following measurements. In total, six sampling campaigns were conducted between 24 February and 17 March 2023, encompassing the period around the first fertilizations (27 and 28 February) and two campaigns later in the season (31 May and 19 July). The sampling was performed around midday (typically between 11:00 and 13:00 local time) to minimize diurnal variability in fluxes. For each chamber and time point, two headspace samples were collected: one immediately after chamber closure (t_0), and one after a 1-hour enclosure period (t_{60}). Air samples were drawn from the chamber headspace with a 60-mL syringe. For subsequent N_2O concentration analysis, 20 mL of the air sample was injected into pre-evacuated 12 mL vials. For stable isotope analyses, 180 mL of the air sample was injected into pre-evacuated 110 mL serum crimp vials. During each sampling campaign, a soil sample was collected for each chamber by combining two soil cores (0-0.1 m depth) taken approximately 0.3 m from the chamber edge. The pooled samples were placed into Schott tubes, which were immediately sealed with Parafilm, enclosed in plastic bags, and stored in a cooling box before being transferred to a freezer at −18 °C. Soil water was later extracted from the samples using cryogenic vacuum distillation (Ehleringer and Osmond, 2000). The stable oxygen isotope ratio ($\delta^{18}O$) of the extracted water was then measured using an isotope ratio mass spectrometer (IRMS; DeltaplusXP, Finnigan MAT, Bremen, Germany) and expressed in the delta notation referenced to the Vienna Standard Mean Ocean Water (V-SMOW) in ‰ (Eq. 2) as:

$$\delta^{18}O = \frac{R_{sample}}{R_{reference}} - 1 \quad (2)$$

where R denotes the ratio of $^{18}O/^{16}O$.

N_2O gas samples were analyzed for their stable N and oxygen isotope ratios ($\delta^{15}N^{bulk}$, $\delta^{18}O$, respectively) and site preference (SP-N_2O) using a trace gas preparation unit (Elementar, Manchester, UK) coupled to an IsoPrime100 IRMS (Elementar, Manchester, UK). Calibration and data correction followed the procedure described in Verhoeven et al. (2019) and in Gallarotti et al. (2021), including the use of multiple working standards and correction for instrumental drift, span, and linearity. Site preference (SP) represents the difference between the N isotope ratios at the central (α) and terminal (β) N positions of the N_2O molecule. Unlike $\delta^{15}N^{bulk}$, SP-N_2O is independent of the initial substrate, making it a more direct indicator of the N_2O production pathway (Toyoda et al., 2002). The isotopic signature of emitted N_2O was calculated using the following two-point mixing equation (Eq. 3):

$$\delta^z X = \frac{[N_2O]_e \cdot \delta^z X_e - [N_2O]_s \cdot \delta^z X_s}{[N_2O]_e - [N_2O]_s} \quad (3)$$

where $[N_2O]_s$ and $[N_2O]_e$ are the N_2O mixing ratios [ppb] at t_0 and t_{60}, respectively, measured using a gas chromatograph equipped with an electron capture detector (456-GC, Scion Instruments, Livingston, WLO, UK), while $\delta^Z X_s$ and $\delta^Z X_e$ are the corresponding isotope ratios (‰). A threshold of 30 ppb in N_2O concentration increase ($\Delta[N_2O] = [N_2O]_e - [N_2O]_s$) was used to exclude flux estimates for which the change in N_2O concentration during the chamber closure was too small to yield reliable isotopic signatures (Harris et al., 2020b). N_2O fluxes on four of the eight sampling dates, March 1, 3, 6, and 17, exceeded this threshold and were subsequently included in the analyses.

https://doi.org/10.5194/egusphere-2026-27
Preprint. Discussion started: 20 January 2026

To determine the main production pathways of N_2O, a dual isotope mapping approach was used, relating i) $\delta^{18}O$-N_2O to SP-N_2O, and ii) $\delta^{15}N^{bulk}$-N_2O to SP-N_2O. The mixing endmembers for nitrification (Ni), bacterial denitrification (bD), nitrifier denitrification (nD), and fungal denitrification (fD) were chosen according to Yu et al. (2020). The $\delta^{18}O$-N_2O endmembers of bD, nD, and fD were adjusted by the mean $\delta^{18}O$ of soil water to account for the oxygen isotopic signature of the substrate (Lewicka-Szczebak et al., 2020). Since no measurements of the $\delta^{15}N$ of soil N precursors were available, a $\delta^{15}N$ value of 0‰ was assumed for precursor nitrate and ammonium in the $\delta^{15}N^{bulk}$-N_2O vs. SP-N_2O map. The contributions of different N_2O production pathways and the residual fraction of unreduced N_2O (r) were estimated with the FRAME software, implementing a Markov Chain Monte Carlo model (Lewicki et al., 2022). The FRAME model was configured using process-specific mean values and fractionation factors from Yu et al. (2020), and the $\delta^{18}O$-N_2O mean values were corrected for $\delta^{18}O$-H_2O.

2.6 Vegetation and soil measurements

Leaf area index (LAI), vegetation height, and phenological development stages were monitored throughout the study. From March to July 2023, measurements were conducted at 2- to 3-week intervals to capture the growth dynamics during the most active vegetative period of winter wheat, and at key developmental stages before and after this period. LAI and canopy height were measured at six locations spread 5 m apart along four transects originating from the EC station (Fig. 1). LAI was measured using a LAI-2000 Plant Canopy Analyzer (LI-COR Biosciences, USA) by taking one above-canopy and six below-canopy readings for each transect. Under clear sky conditions, measurements were conducted towards the North to avoid direct sunlight on the lens. Vegetation height was determined by measuring the height of an expanded polystyrene plate of 0.25 m^2 dropped on top of the vegetation at each spot (Ammann et al., 2007). Phenological development stages of winter wheat were identified according to the BBCH-scale (Meier, 2018) for five plants randomly selected in the field.

Aboveground biomass (AGB) was sampled monthly, using a harvest frame with a defined area of 0.1 m^2. Three samples were randomly collected at each of the four defined field sections (Fig. 1), and entire wheat plants were cut 2 cm above the ground. The dry weight was determined after drying all plant samples at 60 °C for 48 hours. The dried samples were further processed by first cutting the biomass into smaller pieces, then a subsample was ground to a fine powder with a ball mill (MM200, Retsch, Germany). Finally, about 4 mg was weighed into small tin capsules, and carbon (C) and N concentrations (in %) were determined with a Flash EA 1112 elemental analyzer (Thermo Italy, former CE Instruments, Rhodano, Italy).

During the wheat cropping season, soil samples were collected five times using a machine-assisted soil core sampler. The soil samples were collected within the same field sections used for AGB sampling, with ten to fifteen soil cores taken at each section and bulked for each soil depth (0-0.3, 0.3-0.6, and 0.6-0.9 m). Ammonium (NH_4^+) and nitrate (NO_3^-) were extracted by an external laboratory using a 0.01 M $CaCl_2$ solution at a 1:4 soil-to-solution ratio, following the Swiss reference method (Buerge, 2020) established by the Federal Agriculture Research Center, Agroscope. Concentrations were photometrically determined by the same laboratory and reported in mg N per 100 g of dry soil. Soil mineral N (N_{min}) was then calculated in kg N ha^{-1} using the same reference method.

https://doi.org/10.5194/egusphere-2026-27
Preprint. Discussion started: 20 January 2026

Measurements of plant-available soil N complemented soil sampling from March to September 2023. Three Plant Root Simulator sets (17.5 cm^2 surface area each; PRS™, Western Ag, Saskatoon, Canada), each consisting of one anion and one cation exchange resin probe, were buried at 0-0.1 m soil depth. The probes were positioned along the wheat inter-row at the same five locations used for chamber measurements (Fig. 1). The probes were replaced every two to three weeks, resulting in seven burial periods. No probes were buried in June due to technical issues, nor in the second half of July due to tillage and sowing operations. Prior to shipment to Western Ag for analyses, the PRS probes were rinsed with deionized water and stored at 5°C. Extraction of NH_4^+ and NO_3^- with 0.5 mol L^{-1} HCl was conducted by pooling all three PRS sets from each location, yielding one value per location and sampling period (in µg N per 17.5 cm^2 per time of burial). Since all NH_4^+ measurements were below the detection limit (except for one sample), we excluded NH_4^+-N from further analyses.

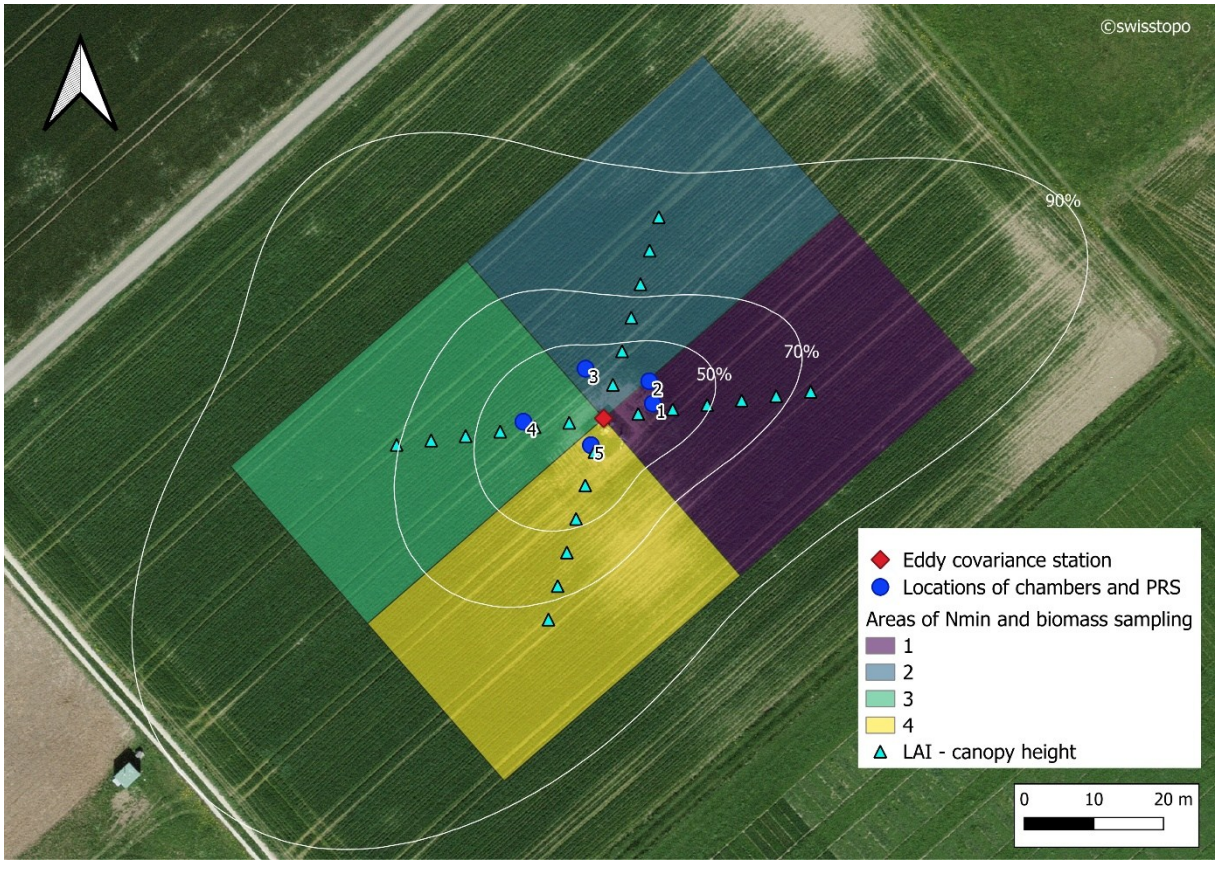

Figure 1. Experimental setup at the study site in Oensingen during the 2022-2023 measurement period. The red diamond marks the eddy covariance station; white lines delineate the 50%, 70%, and 90% average footprint areas (based on the Kljun et al., 2015 model); blue dots indicate locations of manual chambers and plant root simulator (PRS) probes; colored rectangles show areas for Nmin and aboveground biomass sampling; triangles denote fixed locations for LAI and canopy height measurements. Orthophoto: Federal Office of Topography swisstopo.

https://doi.org/10.5194/egusphere-2026-27
Preprint. Discussion started: 20 January 2026

2.7 Investigating the temporal development of N_2O drivers

2.7.1 XGBoost model

To investigate biotic and abiotic drivers of N_2O fluxes, we implemented a regression model based on eXtreme Gradient Boosting (XGBoost; Chen & Guestrin, 2016), using the *xgboost* library in Python. The dataset was aggregated into 4-hour intervals to balance temporal resolution with noise reduction. An initial set of predictors included variables previously identified as key drivers of N_2O fluxes (Butterbach-Bahl et al., 2013; Feigenwinter et al., 2023; Goodrich et al., 2021; Maier et al., 2022, 2025), namely soil temperature, WFPS (at depths of 0.05, 0.15, and 0.3 m), precipitation, time since key management events (soil preparation, fertilization, and harvest), and gross primary productivity (GPP). GPP was selected as the indicator of vegetation performance instead of leaf area index (LAI) and canopy height because of its higher temporal resolution and its strong correlation with aboveground crop N content observed during the winter wheat season (Fig. A1). To represent N availability from fertilization, we included the cumulative N applied over the preceding 30 days (kg N ha^{-1}), a window length that reflects the typical duration of enhanced soil N availability and N_2O emissions following fertilizer application (Bouwman, 1996). In addition, we derived lagged values, rolling means (sums for precipitation and GPP), and first-order time derivatives (i.e., rates of change) for environmental variables, calculated over 12-, 24-, and 48-hour intervals. Recursive feature elimination (Guyon et al., 2002) was applied to systematically identify the most informative predictors from the initial variable set. The cumulative N applied over the preceding 30 days emerged as the strongest important predictor of N_2O fluxes, followed by time since soil preparation, time since fertilization, and the 48-h (preceding) rolling mean of WFPS at 0.3 m depth. To minimize multicollinearity while retaining the key biotic and abiotic drivers, we selected the variable with the highest ranking from each category of predictors. The final set of predictors included: cumulative N applied over the past 30 days, time since fertilization, time since soil preparation, the 48-h (preceding) rolling mean of WFPS at 0.3 m depth, the change in WFPS at 0.3 m depth over the preceding 48 h, the 48-h (preceding) rolling mean of soil temperature at 0.3 m depth, and the cumulative GPP over the preceding 48 h. For WFPS, both its absolute value and short-term temporal change were retained, as they capture distinct dimensions of soil moisture dynamics. Similarly, both cumulative applied N and time since fertilization were included, reflecting their complementary roles in describing N availability and timing of fertilization events.

Following variable selection, model hyperparameters were optimized using 10-fold cross-validation. To account for temporal autocorrelation and avoid overfitting, while also providing representative coverage of the measurement period, we employed a custom time-block strategy. This approach involved an 80/20 split between training and validation, with the validation set comprising randomly selected, non-overlapping time blocks that together represented 20% of the available data. This splitting strategy was consistently applied throughout the modeling workflow, including during cross-validation and final model evaluation. Model performance was evaluated using root mean squared error (RMSE), which quantified the average deviation between predicted and observed values, and the coefficient of determination (R^2), calculated both during cross-validation and for the final model.

https://doi.org/10.5194/egusphere-2026-27
Preprint. Discussion started: 20 January 2026

The final XGBoost model used the following hyperparameter values: colsample_bytree = 1, gamma = 0, learning_rate = 0.05, max_depth = 10, min_child_weight = 2, n_estimators = 100, and subsample = 0.65, and was trained with early stopping (10 rounds) to prevent overfitting. Cross-validation results showed a R^2 of 0.60 and a RMSE of 1.1 nmol N_2O m^{-2} s^{-1} on the validation set, while the training set showed a R^2 of 0.98 and a RMSE of 0.29 nmol N_2O m^{-2} s^{-1}. The final model, trained with early stopping (10 rounds) to prevent overfitting, achieved a R^2 of 0.70 and a RMSE of 1.14 nmol N_2O m^{-2} s^{-1} on the test set (Fig. A2).

2.7.2 SHAP analyses

To interpret model outputs and investigate the temporal dynamics of predictor (i.e., driver) contributions to N_2O fluxes, we applied SHAP (SHapley Additive exPlanations; Lundberg and Lee, 2017), a model-agnostic interpretability framework based on cooperative game theory. SHAP was implemented using the *SHAP* Python library in combination with the XGBoost model trained for N_2O flux prediction. Specifically, we used TreeExplainer (Lundberg et al., 2020), a SHAP implementation optimized for tree-based models such as XGBoost. This method decomposes each model prediction into additive contributions from individual predictors, quantifying how much each one increases or decreases the prediction relative to a defined baseline.

In SHAP analysis, the baseline is defined by the expected prediction over a reference dataset that represents typical input conditions and serves as a reference state for calculating feature contributions (Lundberg et al., 2020; Molnar, 2025). To construct this dataset, we excluded the 30 days following fertilization or soil preparation to best represent average, undisturbed environmental conditions. This ensured that SHAP values reflected the influence of the predictor variables in relation to typical conditions, without being skewed by the absence of recent management events. SHAP values were used to quantify the absolute contribution of each predictor to the model output. For interpretability, SHAP values were then normalized by dividing each SHAP value by the sum of all absolute SHAP values for that prediction. This transformation yielded unitless relative contributions that are independent of prediction magnitude and whose absolute values sum to one across all predictors at each time step, while preserving the direction of each predictor's effect. This enabled a time-resolved assessment of the relative importance of individual predictors.

For interpretation of the SHAP analyses, we grouped related variables by summing their SHAP values to assess the overall contribution of broad driver categories. Specifically, SHAP values for the cumulative N applied and time since fertilization were combined to represent the contribution of fertilization-related drivers, labeled as 'N fertilization'. Likewise, SHAP values for WFPS and its temporal derivative were aggregated to capture the influence of soil moisture dynamics, referred to as 'WFPS'. For clarity, we refer to 'time since soil preparation' as 'soil disturbance'. From this point onward, we will refer to predictor variables as 'drivers' in the manuscript.

All statistical analyses were conducted in Python (version 3.9.13) using NumPy (Harris et al., 2020a), pandas (McKinney, 2010), SciPy (Virtanen et al., 2020), and scikit-learn (Pedregosa et al., 2011). Data visualization was performed with

https://doi.org/10.5194/egusphere-2026-27
Preprint. Discussion started: 20 January 2026

Matplotlib (Hunter, 2007) and Seaborn (Waskom, 2021). The Python scripts used for these analyses and visualizations are available on GitHub and archived on Zenodo (Turco, 2025b).

3. Results

3.1 Environmental conditions and vegetation growth

The cropping season for winter wheat at Oensingen started on 6 October 2022, following a temporary grassland (grass-clover), which was cut on 20 September 2022 (Table 1). Large precipitation events followed this final cut, totaling 103 mm in 15 days (Fig. 2a), resulting in increased WFPS values (Fig. 2b). During this period, topsoil temperature (0.05 m depth) ranged between 12 and 15 °C (Fig. 2c). Throughout the winter wheat growing season, cumulative precipitation amounted to 698 mm. However, rainfall was unevenly distributed, with November to December 2022 and March to April 2023 accounting for 33% and 29% of the total precipitation, respectively (Fig. 2a). A dry spell occurred between late December 2022 and early March 2023, but WFPS in the topsoil remained above 60% (Fig. 2b). In contrast, a second drought period between mid-May and late June 2023 coincided with warmer conditions and led to a decline in WFPS throughout the soil profile (20 to 30% in the top 0.3 m). Topsoil temperature ranged between 0.4 and 24.6 °C and showed a typical temporal course, with lowest values from December 2022 to February 2023 and highest values in July 2023. The development of LAI during the growing season followed the seasonal weather pattern, remaining low throughout winter and early spring before increasing steadily from late March 2023 (Fig. 2d). Canopy development peaked in late May, shortly before anthesis (i.e., flowering; Table A2) in early June 2023. During June's dry and warm conditions, canopy desiccation and signs of water stress became apparent, accompanied by the onset of senescence as seen in the decline of LAI. Crop management started with two fertilization events early in the season (27-28 February 2023) during late tillering (Table A2), approximately one week before the onset of rainfall that ended the winter dry spell. The last fertilization event was conducted during the early stem elongation phase (6 April), following a period of increased temperature. After the harvest of winter wheat in mid-July 2023 (Table 1), the soil was cultivated and a cover crop was sown at the end of July, accompanied by intense rainfall and declining soil temperature. The summer cover crop season was short and characterized by increasing soil moisture, particularly in the deeper soil layers (0.3-0.5 m; Fig. 2b), and by gradually decreasing soil temperature (Fig. 2c). The season ended with mulching and soil cultivation at the end of September (Table 1), after which the soil was left bare until the sowing of the next crop on 4 October 2023.

https://doi.org/10.5194/egusphere-2026-27
Preprint. Discussion started: 20 January 2026

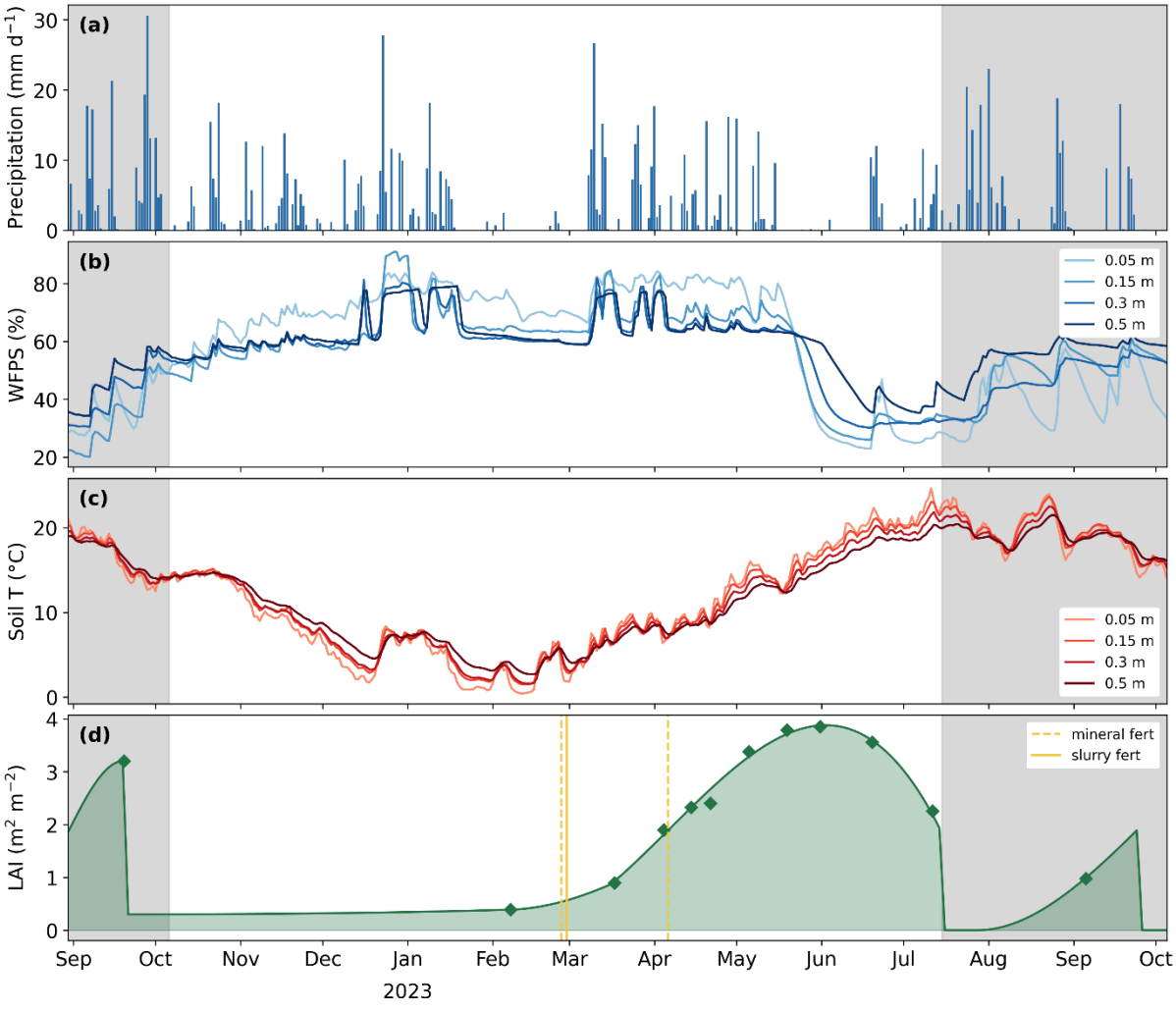

Figure 2. Environmental conditions and vegetation dynamics at the Oensingen cropland from September 2022 to October 2023. The unshaded area corresponds to the winter wheat cropping season, while the shaded areas indicate the final phase of the preceding temporary grassland and the cover crop following the winter wheat harvest. (a) Daily precipitation sums; (b) daily average water-filled pore space (WFPS) at 0.05, 0.15, 0.3, and 0.5 m soil depths; (c) daily average soil temperature (soil T) at the same depths as WFPS; (d) leaf area index (LAI), with diamonds indicating measured values and the line representing modeled values obtained using cubic splines. Yellow lines indicate fertilization (fert) events.

3.2 Greenhouse gas fluxes

3.2.1 Net ecosystem CO_2 exchange (NEE)

During the final regrowth phase of the temporary grassland in October 2022, daily mean NEE fluctuated around zero (-2.2 to +3.9 µmol m^{-2} s^{-1}; Fig. 3a). After the final grassland cut, NEE became positive, indicating a net release of CO_2. Two weeks later, an herbicide application followed by direct seeding of winter wheat further increased NEE, which reached a daily mean of +6.1 µmol m^{-2} s^{-1}. In late October 2022, NEE gradually declined in response to decreasing soil temperature (Fig. 2c) and

https://doi.org/10.5194/egusphere-2026-27
Preprint. Discussion started: 20 January 2026

remained low but positive during the winter months (December - February), reflecting a small net release of CO_2. From early to late March 2023, daily mean NEE decreased from +2.3 to -3.5 µmol m^{-2} s^{-1}, indicating the onset of net CO_2 uptake. During peak crop growth in early May, daily mean NEE reached -10.5 µmol m^{-2} s^{-1}, and the most negative half-hourly flux (QC0) was -48.2 µmol m^{-2} s^{-1}. With the onset of crop anthesis at the end of May (Table A2) and the occurrence of dry soil conditions (Fig. 2b), NEE steadily increased, consistent with reduced photosynthetic CO_2 uptake, typical of this phenological phase in winter wheat. A small CO_2 emission peak, with daily mean NEE reaching up to +3.7 µmol m^{-2} s^{-1}, occurred in late June following rewetting after an extended dry period. From July to late August 2023, daily mean NEE remained positive (+1.9 to +7.7 µmol m^{-2} s^{-1}), indicating net CO_2 release during wheat maturation as well as after harvest and subsequent early cover crop establishment. In late August 2023, NEE was negative again, reflecting net CO_2 uptake due to the successful establishment of the cover crop. Directly after mulching of the cover crop and soil cultivation in late September, the field became a net CO_2 source again (positive NEE).

3.2.2 Net ecosystem N_2O fluxes

Net N_2O fluxes showed pronounced temporal variations, with very low fluxes during winter 2022/2023 and highest emissions during crop establishment and after fertilization events. During the final grassland regrowth phase, daily mean N_2O fluxes were negligible (-0.3 to +0.6 nmol m^{-2} s^{-1}; Fig. 3a), but increased markedly after winter wheat seeding, reaching a daily mean of +5.7 nmol m^{-2} s^{-1} on 22 October 2022 (Fig. 3b). This peak occurred after rainfall increased topsoil (0.05 m) WFPS from 51 to 62% (Fig. 2b), when soil temperature exceeded 14 °C (Fig. 2c), and LAI was below 1 m^2 m^{-2} (Fig. 2d). Throughout winter (December 2022 - February 2023), N_2O fluxes remained near zero, with daily means ranging from -0.1 to +0.9 nmol m^{-2} s^{-1}. Following the first fertilization events (27-28 February), providing a total of 111 kg N ha^{-1} (Table 1), N_2O fluxes exhibited three distinct peaks in March 2023. The first peak occurred shortly after fertilization, with a daily mean flux of +6.2 nmol m^{-2} s^{-1} on 2 March 2023, under conditions of topsoil WFPS above 65%, soil temperature below 5 °C, and LAI still below 1 m^2 m^{-2}. A second peak followed approximately ten days later, reaching a daily mean flux of +13.6 nmol m^{-2} s^{-1} on 12 March and a maximum half-hourly flux (QC0) of +27.8 nmol m^{-2} s^{-1}. The last peak occurred between 25 and 29 March, reaching a daily mean flux of +4.0 nmol m^{-2} s^{-1} on 28 March. These second and third peaks were preceded by precipitation events that raised topsoil WFPS above 80%, with soil temperature ranging from 5 to 10 °C, while LAI exceeded 1 m^2 m^{-2} only during the last peak. Following the final fertilization event on 6 April (27 kg N ha^{-1}; Table 1), net ecosystem N_2O fluxes increased again, with daily mean values reaching +5.1 nmol m^{-2} s^{-1} on 14 April 2023. Although less pronounced than the March peaks, this emission event likewise followed rainfall that increased WFPS above 80% (Fig. 2b), but occurred under a more developed canopy, with LAI being nearly double than that during the March peaks (Fig. 2d). During peak crop growth period, when LAI increased from 2.5 to 4 m^2 m^{-2} (mid-April to late May; Fig. 2d), daily mean N_2O fluxes remained negligible (-0.4 to +1.4 nmol m^{-2} s^{-1}), despite high WFPS values (above 60% throughout the soil profile) and increasing soil temperatures. A short-lived emission event occurred after rewetting on 19 June, following a drought in May/June 2023. Despite WFPS remaining below 40%, daily mean N_2O fluxes reached +11.2 nmol m^{-2} s^{-1} on 20 June, with a

https://doi.org/10.5194/egusphere-2026-27
Preprint. Discussion started: 20 January 2026

maximum half-hourly flux (QC0) of +21.6 nmol m^{-2} s^{-1}, at a time when LAI was already declining following anthesis (Table A2). In July, during the final stages of wheat maturation and after harvest, daily mean N_2O fluxes remained low but positive (0.0 to +3.1 nmol m^{-2} s^{-1}). A distinct peak occurred in late July, shortly after the cover crop was sown, with a daily mean flux of +7.3 nmol m^{-2} s^{-1} on 30 July. Emissions remained low in August (0.0 to +2.3 nmol m^{-2} s^{-1}) but rose slightly following mulching of the cover crop and subsequent soil cultivation in late September 2023.

3.2.3 Net ecosystem CH_4 fluxes

Net CH_4 fluxes remained low throughout the measurement period, typically indicating small CH_4 emissions, with daily average fluxes ranging from -7.0 to +28.5 nmol CH_4 m^{-2} s^{-1} (Fig. 3c). No consistent temporal patterns were evident, although slightly elevated fluxes indicating net CH_4 release were recorded from mid-October to early November 2022 and in early January 2023 (Fig. 2).

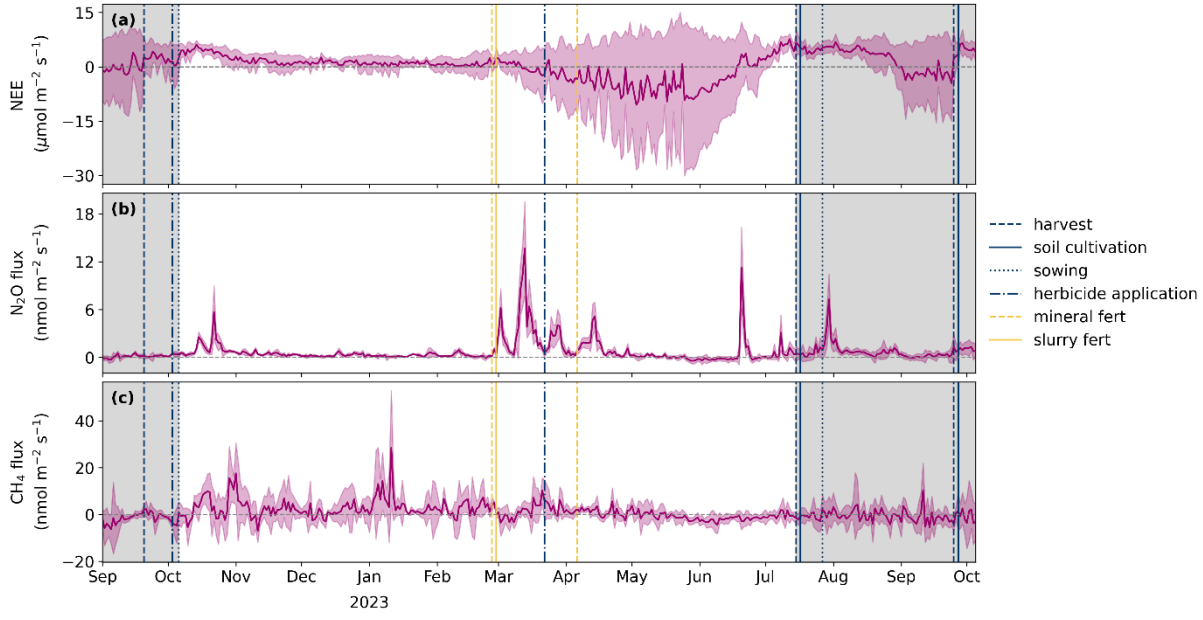

Figure 3. Gap-filled greenhouse gas fluxes at the Oensingen cropland measured from September 2022 to October 2023. The unshaded area corresponds to the winter wheat cropping season, while the shaded areas indicate the final phase of the preceding temporary grassland and the cover crop following winter harvest. (a) Net ecosystem CO_2 exchange (NEE), (b) net ecosystem N_2O fluxes, and (c) net ecosystem CH_4 fluxes. Fluxes were gap-filled using the Marginal Distribution Sampling (MDS) for NEE and random forest (RF) for N_2O and CH_4 fluxes. Lines represent daily averages of the gap-filled half-hourly fluxes, while the shading indicates ± 1 standard deviation. Vertical lines mark management activities: yellow dashed = mineral fertilization (fert), yellow solid = slurry fertilization (fert), blue solid = soil cultivation, blue dotted = sowing, blue dashed = harvest, and blue dash-dot = herbicide application. See Table 1 for details on management activities.

3.3 N_2O emission factor and greenhouse gas budgets

During the winter wheat cropping season (282 days), cumulative N_2O emissions were 5.5 kg N_2O-N ha^{-1} (Table 2), with an average gap-filled flux of 0.81 nmol m^{-2} s^{-1}. When scaled to crop yield, this corresponded to 1.1 kg of N_2O-N emitted per

https://doi.org/10.5194/egusphere-2026-27
Preprint. Discussion started: 20 January 2026

ton of wheat grain (dry matter). A background N_2O flux of 0.44 nmol m^{-2} s^{-1} was calculated as the average of gap-filled fluxes outside the 30-day post-fertilization periods, thereby minimizing the influence of short-term fertilization-induced peaks. Accounting for this background flux, the N_2O cumulative flux due to fertilization-induced emissions amounted to 2.5 kg N_2O-N ha^{-1} during the winter wheat cropping season, accounting for approximately 45% of the total N_2O emissions. Based on a total N input from fertilizers of 138 kg N ha^{-1} (Table 1), the resulting emission factor (EF) was 1.8%. During the subsequent 60-day cover crop season, cumulative N_2O emissions reached 1.1 kg N_2O-N ha^{-1}, and the average daily sum of N_2O emissions (17.6 g N_2O-N ha^{-1} d^{-1}) was only slightly lower than that observed during the winter wheat season (19.6 g N_2O-N ha^{-1} d^{-1}).

Throughout the winter wheat cropping season, the ecosystem acted as a net CO_2 sink, with a cumulative NEE of -89 g CO_2-C m^{-2} (Table 2). However, this climate benefit was largely offset (~ 70%) by concurrent net N_2O emissions, while net CH_4 emissions remained negligible. In contrast, the cover crop acted as a net CO_2 source, emitting 108 g CO_2-C m^{-2}. Net N_2O emissions during this period accounted for approximately 10% of the total GHG budget, while the net CH_4 sink was again negligible. The difference in NEE between the two crops was reflected in their respective GHG budgets: winter wheat resulted in a net GHG sink of -76 g CO_2-equivalents (CO_2-eq) m^{-2}, while the cover crop resulted in a net GHG source of 441 g CO_2-eq m^{-2}. The difference between the two crops was even more striking when comparing their daily sums of CO_2-eq, with winter wheat averaging -0.27 g CO_2-eq m^{-2} d^{-1} and the cover crop averaging +7.4 g CO_2-eq m^{-2} d^{-1}, resulting in a daily difference of approximately 8 g CO_2-eq m^{-2} d^{-1} (Table 2).

Table 2. Cumulative greenhouse gas (GHG) fluxes and daily average sums for the winter wheat and the cover crop cropping seasons (282 and 60 days, respectively), shown separately for the three gases CO_2, N_2O, and CH_4, as well as the GHG budget (sum of all three gases). No C inputs or exports (fertilization, harvest) are included in the flux budget. Negative values indicate net uptake, while positive values represent net release of CO_2, N_2O, and CH_4 to the atmosphere. CO_2-equivalents (g CO_2-eq m^{-2}) for N_2O and CH_4 were calculated using global warming potentials (GWP_{100}) of 273 and 27, respectively, applied to fluxes expressed in g m^{-2} (IPCC, 2021).

		Winter wheat (282 days)	Cover crop (60 days)
CO_2	Cumulative (g CO_2-C m^{-2})	-89	+108
	Cumulative (g CO_2-eq m^{-2})	-329	+397
	Daily (g CO_2-eq m^{-2} d^{-1})	-1.17	+6.62
N_2O	Cumulative (kg N_2O-N ha^{-1})	+5.5	+1.1
	Cumulative (g CO_2-eq m^{-2})	+237	+45
	Daily (g CO_2-eq m^{-2} d^{-1})	+0.84	+0.76
CH_4	Cumulative (g CO_2-C m^{-2})	+0.45	-0.03
	Cumulative (g CO_2-eq m^{-2})	+16	-1
	Daily (g CO_2-eq m^{-2} d^{-1})	+0.06	-0.02
GHG budget	Cumulative (g CO_2-eq m^{-2})	-76	+441

https://doi.org/10.5194/egusphere-2026-27
Preprint. Discussion started: 20 January 2026

	Daily (g CO_2-eq m^{-2} d^{-1})	-0.27	+7.35

3.4 Drivers of N_2O flux dynamics over time

3.4.1 Temporal development of N_2O flux driver contributions

We used SHAP to quantify both the magnitude and direction (positive or negative) of each driver's contribution to net ecosystem N_2O fluxes across all three crops, relative to a reference state (baseline). In our case, the baseline represents the model's expected N_2O flux under rather undisturbed conditions (avoiding post-fertilization and post-soil management periods) and was estimated as 0.27 nmol m^{-2} s^{-1} using a subset of the data (see Sect. 2.7.2). This baseline value was lower than the N_2O background flux given above, since we also excluded post-soil management periods. To assess the overall influence of each driver across the study period, we summed the SHAP values over time, but separately for positive and negative contributions. This approach avoided cancelling opposing effects and revealed how strongly each driver enhanced or decreased N_2O emissions (Fig. A3). N fertilization and soil disturbance increased the N_2O fluxes (i.e., positive SHAP values) relative to the baseline. In contrast, soil moisture, soil temperature, and GPP exhibited both positive and negative SHAP values, reflecting their capacity to either increase or decrease N_2O fluxes depending on environmental conditions. Across the study period (September 2022 - October 2023), N fertilization was the dominant driver increasing N_2O fluxes (37% of all positive contributions), while soil moisture (23%), soil disturbance (16%), GPP (14%), and soil temperature (10%) also contributed to positive deviations from the baseline flux. Conversely, soil moisture (48% of all negative contributions), soil temperature (28%), and GPP (24%) showed substantial negative contributions, indicating periods when these variables reduced N_2O fluxes relative to the baseline.

To assess the relative influence of each driver in a time-resolved manner and independently of the absolute magnitude of predictions, we computed daily averages of normalized SHAP values (see Sect. 2.7.2). These relative driver contributions revealed distinct temporal patterns across the study period (September 2022 - October 2023; Fig. 4). In September 2022, during the final grassland regrowth phase, N_2O emissions were mainly suppressed by WFPS (negative relative contributions; Fig. 4), although GPP exerted a positive effect later in the month. At the beginning of October, herbicide application and the direct seeding of wheat introduced soil disturbance, and N_2O fluxes during crop establishment were primarily driven by soil disturbance and GPP (positive relative contributions; Fig. 4). Throughout winter (November 2022 - February 2023), soil temperature consistently suppressed N_2O emissions (negative relative contributions), while GPP maintained a positive effect. In spring (March - April 2023), which corresponded to the period of highest observed N_2O fluxes (Fig. 4a), emissions were primarily driven by N fertilization, followed by WFPS. Later in the season, when photosynthetic activity and presumably plant N demand increased (April), the effect of GPP shifted towards decreasing N_2O fluxes. The low N_2O emissions observed from May to mid-June were thus strongly driven by large negative effects of soil temperature, GPP, and WFPS (Fig. 4b). In contrast, during grain filling and post-harvest (July to mid-August), the SHAP analysis indicated that soil

https://doi.org/10.5194/egusphere-2026-27
Preprint. Discussion started: 20 January 2026

temperature and soil disturbance strongly increased N_2O emissions, while GPP had a smaller but still positive effect. Following the establishment of the cover crop in September, the effect of GPP became negative again, coinciding with an increase in photosynthetic CO_2 uptake.

To investigate the changing role of GPP in more detail, we focused on the winter wheat period from March 2023 to harvest (mid-July 2023), thereby limiting potential confounding factors (Fig. 5). In this period, N_2O fluxes were negatively related to GPP, suggesting that high photosynthetic activity (high GPP) was associated with low N_2O emissions. This relationship was modulated by WFPS: the decline in N_2O fluxes with increasing GPP was weakest in the driest WFPS class (≤ 55%) and became progressively stronger at higher soil moisture, as indicated by increasingly negative regression slopes (R^2 = 0.28, 0.62, and 0.80; all $p < 0.001$; Fig. 5).

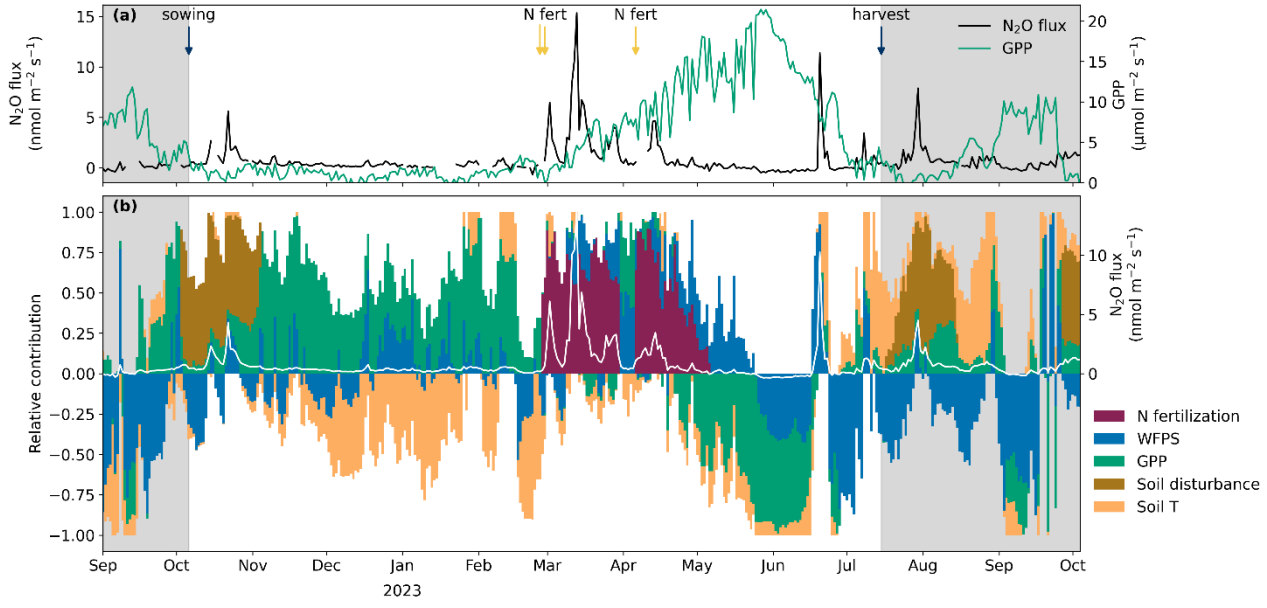

Figure 4. Temporal dynamics of N_2O fluxes, gross primary productivity (GPP), and relative driver contributions to N_2O fluxes at the Oensingen cropland from September 2022 to October 2023. The unshaded area corresponds to the winter wheat cropping season, while the shaded areas indicate the final phase of the preceding temporary grassland and the cover crop following winter harvest. (a) Daily average N_2O fluxes (measured, highest quality fluxes only) are shown in black, and daily average GPP in green. Arrows at the top denote management activities conducted during the winter wheat cropping season. (b) Relative contributions of individual drivers (i.e., N fertilization, water-filled pore space (WFPS), GPP, soil disturbance, and soil temperature (soil T)) are expressed as daily averages of normalized SHAP values (see Sect. 2.6.2 for methodological details). The baseline (SHAP = 0) corresponds to a predicted N_2O flux of 0.27 nmol m^{-2} s^{-1}. Positive values indicate a driver's increasing effect on N_2O fluxes, while negative values reflect a decreasing effect. The white line represents the model-predicted N_2O flux.

https://doi.org/10.5194/egusphere-2026-27
Preprint. Discussion started: 20 January 2026

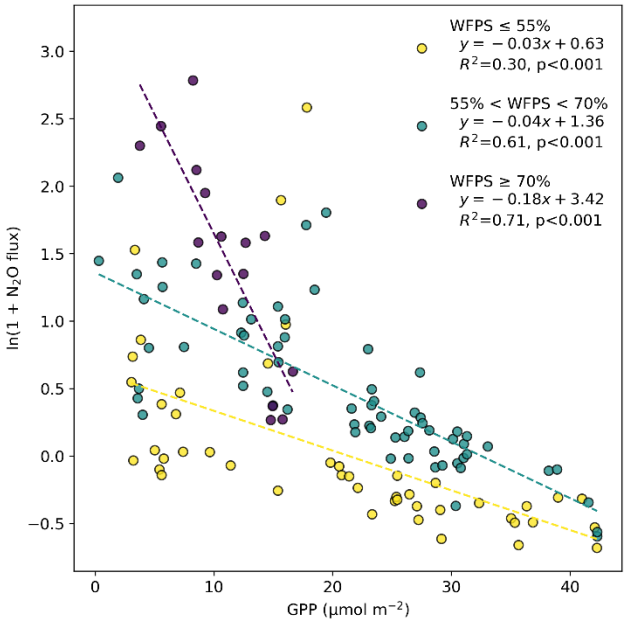

Figure 5. Relationship between gross primary productivity (GPP; rolling sum over the preceding 48 h) and the measured N_2O fluxes (QC0 only, daily averages) between March and mid-July 2023 in winter wheat. Points are colored by water-filled pore space classes (WFPS; at 0.3 m soil depth), based on the 48-h rolling mean of WFPS (same window as for GPP). Dashed lines show the linear regressions for each class, with the corresponding regression statistics given as well.

3.4.2 Soil available nitrogen

To assess soil N availability to roots and microorganisms, we used two complementary approaches: (i) time-integrated supply of plant-available NO_3^--N measured with PRS probes, and (ii) instantaneous mineral N supply (N_{min}), derived from soil-extractable NO_3^- and NH_4^+ concentrations in the 0-0.3 m soil layer. N_2O fluxes increased significantly with soil mineral N availability, both for integrated (Fig. 6c, R^2 = 0.61; $p<0.05$) and instantaneous supply (Fig. 6d; R^2 = 0.77; $p<0.05$). The lowest N_2O emissions occurred during periods of highest GPP (point 4 in Fig. 6c; point D in Fig. 6d) or without prior fertilization events (points A and B in Fig. 6d). In contrast, the highest N_2O emissions occurred after fertilization events, when soil mineral N availability was highest (points 1 and 2 in Fig. 6c; point C in Fig. 6d), with average Nmin values reaching 74 kg N ha^{-1} ten days after the first fertilization. Between these extremes, intermediate N availability was observed in December 2022 (point A in Fig. 6d) and in August 2023 during the post-harvest period (points 6 and 7 in Fig. 6c; point E in Fig. 6d). While in August the intermediate N availability coincided with higher N_2O emissions, this was not the case in December, when soil temperature at 0.05 m depth ranged between 3 and 5 °C during the sampling week.

https://doi.org/10.5194/egusphere-2026-27
Preprint. Discussion started: 20 January 2026

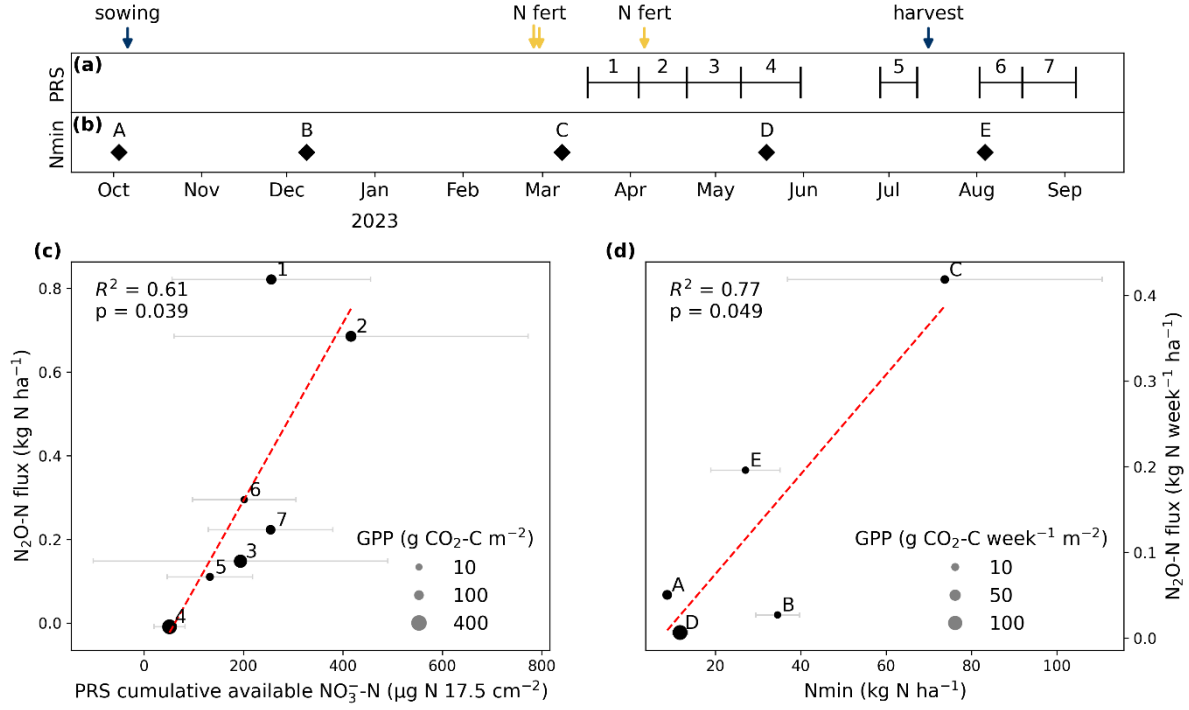

Figure 6. Relationships between nitrogen (N) availability and N_2O fluxes. (a) Timeline of burial periods for plant root simulators (PRS) probes, and (b) of soil mineral N (N_{min}) sampling campaigns. Sowing, harvest, and fertilization dates are also provided. (c) Relationship between cumulative available NO_3^--N (µg N 17.5 cm^{-2}, based on PRS probes) and cumulative N_2O fluxes over the corresponding burial period (15 to 21 days). Means and ± 1 standard deviation are given (n=5). Circle size reflects cumulative GPP during the same period. Numbers indicate the corresponding period as shown in panel (a). A linear regression is shown as a dashed red line, together with the coefficient of determination (R^2) and corresponding p-value. (d) Relationship between N_{min} (0-0.3 m soil depth) and cumulative N_2O fluxes during the week centered on the soil sampling (± 3.5 days). Means ± 1 standard deviation are given (n= 4; except for 1st sampling with no replicates). Circle size reflects cumulative GPP during the same period. Letters indicate the corresponding period as shown in panel (b). A linear regression is shown as a dashed red line, together with the coefficient of determination (R^2) and corresponding p-value.

3.5 N_2O sources using stable isotopes

We used stable oxygen and nitrogen isotopes to identify the microbial processes underlying the measured N_2O fluxes. The $\delta^{18}O$ in N_2O ranged between 17.3 and 39.8‰, while the site preference (SP-N_2O) ranged from -7.2 to +18.2‰ (Fig. 7a). The dual isotope plots suggested that denitrification and/or nitrifier denitrification were the dominant N_2O production pathways during the three weeks following the fertilization events on 27 and 28 February 2023 (Fig. 7a; Fig. A5). Moreover, the observed trend of increasing enrichment of $\delta^{18}O$ and SP-N_2O over time (Fig. 7a) suggested isotopic fractionation associated with the microbial reduction of N_2O to N_2 during denitrification. Results from the FRAME model supported the qualitative source attribution derived from the isotopic mapping approach and enabled the quantification of the relative contributions of individual N_2O-producing processes. While N_2O fluxes slowly decreased over time (Fig. 7b), the contributions of these processes also changed over time. Bacterial denitrification and nitrifier denitrification together accounted for approximately 90% of N_2O production (Fig. 7c), except on 1 March, when nitrification and/or fungal denitrification contributed up to 20%

https://doi.org/10.5194/egusphere-2026-27
Preprint. Discussion started: 20 January 2026

of the total. Moreover, the gradual increase of the reduced N_2O fraction over time (Fig. 7c) indicated a shift toward more complete denitrification, which coincided with a decrease in N_2O fluxes (Fig. 7b).

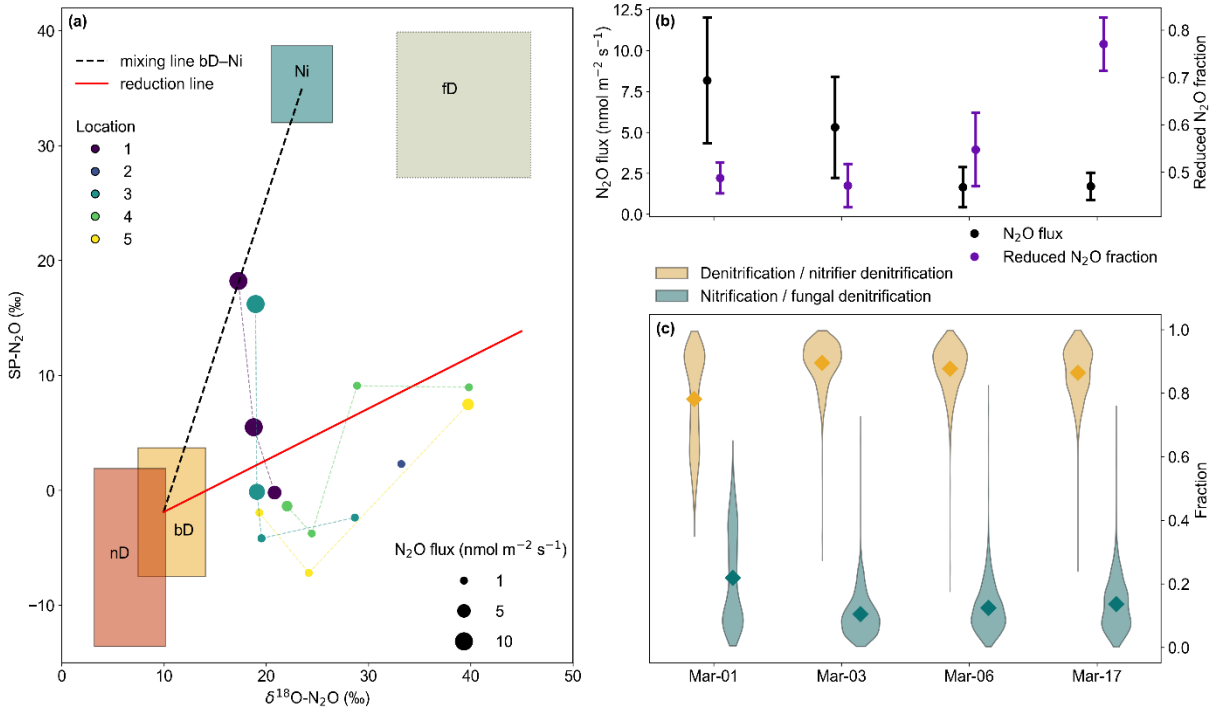

Figure 7. Isotopic signature of N_2O, N_2O flux magnitudes, and their estimated source fractions in March 2023, following fertilization applied on 27 February (ammonium-nitrate) and 28 February (slurry). (a) Dual isotope plot of $\delta^{18}O$-N_2O vs. site preference (SP-N_2O). Colored boxes denote endmembers for the N_2O mixing (nD: nitrifier denitrification, bD: bacterial denitrification, Ni: nitrification, fD: fungal denitrification). Endmember values of boxes are derived from Yu et al. (2020) and adjusted to the values of soil water ($\delta^{18}O$-H_2O = - 9.2‰) at the study site (except for the Ni box). Lines for mixing (black) and N_2O reduction to N_2 (red) are shown. Individual measurements are shown as circles, with size reflecting flux magnitude and color indicating location (1 to 5; see Fig. 1). (b) N_2O fluxes measured with static chambers (black) and reduced N_2O fractions estimated by the FRAME model (purple). Values represent means ± one standard error across measurement locations. (c) N_2O source fractions estimated by the FRAME model for denitrification & nitrifier denitrification and nitrification & fungal denitrification, displayed as violin plots, with mean values indicated by diamonds (see text for details).

4. Discussion

4.1 Seasonal changes in N_2O fluxes and their drivers

The central aim of this study was to determine when and how different biophysical and management factors influenced N_2O fluxes during a winter wheat cropping season, to uncover seasonal patterns in the contributions of each driver. Two periods emerged as particularly sensitive to net N_2O emissions: crop establishment and early spring. Elevated N_2O emissions during the establishment phase of winter wheat were primarily driven by soil disturbance and low GPP. Low GPP reflected limited plant N uptake, while soil disturbance, resulting from herbicide termination of the temporary grassland and direct seeding of winter wheat, likely stimulated mineralization of soil organic matter and crop residues. This was supported by an increase in

https://doi.org/10.5194/egusphere-2026-27
Preprint. Discussion started: 20 January 2026

net ecosystem exchange of CO_2 (NEE), indicating intensified soil respiration. Furthermore, soil N_{min} increased from 8.7 kg N ha^{-1} before crop seeding to 34.6 kg N ha^{-1} by early December 2022 (0-0.3 m soil depth; Fig. 6d), indicating elevated N availability due to low plant N uptake and enhanced N mineralization, consistent with previous observations after herbicide termination of grassland swards from Buchen et al. (2017) and Helfrich et al. (2020). A similar pattern was also observed during cover-crop establishment after wheat harvest: although wheat residues had a lower N concentration (%N) than grassland residues (including clover), elevated soil temperature and mechanical disturbance during post-harvest operations likely enhanced mineralization of soil organic matter (Grandy and Robertson, 2006). This was supported by an increase in soil N_{min} from 12 kg N ha^{-1} in late May to 27 kg N ha^{-1} in early August (0-0.3 m soil depth; Fig. 6d). Thus, different management practices leading to no or reduced vegetation performance favor N_2O emissions.

The high N_2O emissions in early spring were predominantly driven by N fertilization, with WFPS contributing significantly during peak emission events, while GPP consistently decreased emissions from mid-April onward. The first fertilizer applications in late February supplied a large N input (111 kg N ha^{-1}) during the early crop development stage (tillering) and coincided with high soil moisture, conditions typical of central European climates (Ruosteenoja et al., 2018). At this stage, both LAI (Fig. 2d) and photosynthetic CO_2 assimilation rates (Fig. 4a) were still low, indicating limited plant N uptake typical of early growth stages in Swiss winter wheat systems (Argento et al., 2022). These conditions resulted in excess N availability, with soil N_{min} reaching 74 kg N ha^{-1} (0-0.3 m soil depth; Fig. 6d), which, in combination with precipitation events that increased WFPS (Fig. 2b), created optimal conditions for microbial N_2O production. By contrast, the final fertilization in early April 2023 involved a smaller N input (27 kg N ha^{-1}) and was timed to coincide with the stem elongation phase, when plant N demand is typically very high. This is supported by higher LAI (~ 2 m^2 m^{-2}; Fig. 2d) and higher GPP (Fig. 4a), indicative of active growth and greater N assimilation. Under these conditions, less mineral N was likely available for microbial activity, reducing substrate availability for N_2O production and resulting in significantly lower N_2O losses.

Over the entire study period, nitrogen (N) fertilization emerged as the dominant positive driver of N_2O fluxes (Fig. A3), consistent with its role as the primary source of reactive nitrogen in croplands (Shcherbak et al., 2014). However, substantial and temporally dynamic contributions of soil moisture (WFPS), gross primary productivity (GPP), soil temperature, and soil disturbance highlighted the multifactorial nature of N_2O emissions and the need to consider both biophysical and management drivers, along with their complex interactions. Overall, WFPS exhibited both positive and negative effects, but consistently emerged as a key driver during peak N_2O emission events. GPP, used as a proxy for crop N uptake, showed a clear negative relationship with N_2O fluxes: low GPP was associated with elevated N_2O emissions, while sustained photosynthetic activity decreased emissions (Fig. 5). This supported earlier observations that active crop growth competes with microbial processes for soil available N, thereby limiting N_2O production (Feigenwinter et al., 2023; Maier et al., 2022; Timilsina et al., 2024). Further evidence was found in the observed decline in soil N availability during periods of high GPP, particularly in late May (Fig. 6), suggesting efficient crop N uptake. Interestingly, the limiting effect of GPP on N_2O fluxes appeared to be strongly modulated by soil moisture, with larger limitations, i.e., steeper negative slopes observed under

https://doi.org/10.5194/egusphere-2026-27
Preprint. Discussion started: 20 January 2026

higher WFPS conditions (Fig. 5). This provided additional evidence that plant N uptake plays a critical role in mitigating emissions under environmental conditions favorable for N_2O production.

4.2 N_2O emission factor and greenhouse gas budgets

In this study, an EF of 1.8% was estimated for winter wheat, slightly exceeding the IPCC (2019) default value of 1.6% for synthetic N fertilizers in wet climates (Table 2). However, in our study, approximately 30% of the applied N was derived from organic fertilizer applied as slurry, for which the IPCC recommends a lower EF of 0.6%. When accounting for the mixed N sources, the weighted IPCC default EF for our cropping system is 1.3%, indicating that the observed EF exceeded this value by 0.5 percentage points. Cumulative N_2O emissions during the winter wheat season were 5.5 kg N_2O-N ha^{-1}, substantially exceeding the ranges reported for winter wheat by Garnier et al. (2024) for northern France (0.1 - 2.7 kg N_2O-N ha^{-1}) and by Tallec et al. (2022) for southwestern France (0.95 - 2.91 kg N_2O-N ha^{-1}), both studies using chamber measurements, although our N input (138 kg N ha^{-1}) was within their input ranges. Yield-scaled N_2O emissions in our study (1.1 kg N_2O-N Mg^{-1}) were approximately three times higher than the global wheat values reported by Yao et al. (2024) (0.301 - 0.346 kg N_2O-N Mg^{-1}). These discrepancies may partly reflect methodological differences, as global meta-analyses predominantly compile chamber-based flux measurements, which typically have lower temporal and spatial resolutions than the continuous EC flux measurements used in our study. High-frequency EC measurements are valuable for capturing short-lived N_2O emission peaks and for integrating the highly dynamic N_2O fluxes over a larger spatial area than chamber measurements. Despite higher equipment costs and computational requirements, EC measurements thus improve the representativeness and the accuracy of cumulative N_2O loss estimates. To our knowledge, this is the first study to report EC-based N_2O fluxes over a complete winter wheat cropping season. Notably, emissions from winter wheat only slightly exceeded those observed for maize in Switzerland (4.8 kg N_2O-N ha^{-1}; Maier et al., 2022), despite a much shorter cropping season of maize (127 days) compared to that of winter wheat (282 days; about 2.2 times longer). The two crops also clearly differed in their N use efficiency (NUE), calculated as the ratio between N output to N input, with winter wheat taking up 162 kg N ha^{-1} from an input of 138 kg N ha^{-1} (NUE = 117%), whereas maize took up only 56 kg N ha^{-1} from an input of 110 kg N ha^{-1} (NUE = 51%). The higher NUE observed for wheat is consistent with findings from Yu et al. (2022) and can be due to many factors, including crop-specific differences in N use (e.g., related to C3 vs. C4 photosynthetic types), soil N pools and N dynamics (e.g., mineralization rates), as well as weather conditions, affecting plant growth and N_2O emissions.

The substantial N_2O losses significantly affected the total GHG budget of the winter wheat season, with N_2O emissions offsetting 70% of the climate benefit gained from net CO_2 uptake. The offset was considerably higher than reported by Maier et al. (2022) for pea and maize in Switzerland (12% and 10%, respectively), and it also exceeds values reported for managed permanent grasslands in Central Europe, where combined N_2O and CH_4 emissions offset about 21% of CO_2 uptake (Hörtnagl et al., 2018). This large difference is most probably related to the small net CO_2 sink during the winter wheat season, as the ecosystem acted as a net CO_2 source for approximately five months, namely from seeding to mid-March. In contrast, spring-sown pea and maize did not undergo a winter phase; thus, net CO_2 release occurred only briefly during their

https://doi.org/10.5194/egusphere-2026-27
Preprint. Discussion started: 20 January 2026

respective cropping seasons, overcompensated by fast growth and thus high CO_2 uptake during the summer months. Since, to our knowledge, full GHG budgets for winter wheat under temperate conditions are lacking, our study helps to close this gap by providing a season-long, field-scale budget based on continuous flux measurements.

Despite the absence of fertilizer application, the average N_2O flux during the cover crop season was only slightly lower than that observed during the winter wheat season (0.72 vs. 0.81 nmol m^{-2} s^{-1}, respectively). This unexpectedly small difference may be explained by the slow crop establishment during the short cover crop season (60 days), resulting in low plant N uptake, while warm summer temperatures combined with recent soil disturbance from soil preparation enhanced N mineralization of soil organic matter and residues. Recent studies have shown that bare-soil conditions can promote N_2O emissions due to reduced plant N uptake and enhanced microbial activity (Maier et al., 2025; Shang et al., 2024; Tallec et al., 2022; Timilsina et al., 2024), which aligns well with our observations. Moreover, daily mean NEE remained positive until late August (Fig. 3a), indicating that the soil acted as a net CO_2 source for approximately half of the 60-day cover crop season. As a result, the cover crop season was characterized by net CO_2 release, accounting for 90% of the total GHG budget during this period (Table 2). The remaining 10% was attributed to N_2O emissions, as CH_4 fluxes were negligible. Nevertheless, the cover crop season was beneficial for the overall GHG budget at the Oensingen cropland site. In 2019, the soil remained bare after the winter wheat harvest until the sowing of winter barley and no cover crop was sown. As a result, the post-harvest daily CO_2-eq fluxes were approximately double (16 g CO_2-eq m^{-2} d^{-1} over bare soil; Maier et al., 2025) compared to those measured in this study (7.4 g CO_2-eq m^{-2} d^{-1} over cover crop). These elevated GHG emissions were primarily driven by increased CO_2 emissions, with N_2O contributing to a lesser extent. Although management and climatic conditions differed between the two years, this pronounced difference in GHG budgets highlights the benefit of maintaining a green cover crop in summer, between two winter crops, to reduce the GHG footprint of crop production. This interpretation is consistent with findings from Emmel et al. (2018), who showed through modelling that cover crops reduced CO_2 losses compared with bare soil at the same site. These results also align with current Swiss policy efforts (Art. 71c DZV, Swiss Federal Council, 2025), aimed at limiting post-harvest bare-soil periods and promoting continuous soil cover to reduce erosion, improve soil fertility, and nitrate losses to ground water.

4.3 Temporal dynamics of N_2O source processes

The FRAME model by Lewicki et al. (2022) provided a powerful framework for quantifying the relative contributions of different N_2O-producing processes over time. In our study, denitrification and/or nitrifier denitrification were the dominant sources of N_2O production (Fig. 7). Interestingly, nitrification and/or fungal denitrification contributed most strongly immediately after N fertilization (~20%), but declined rapidly thereafter, indicating that nitrification was only a short-lived contributor while denitrification remained dominant (Fig. 7). This transient response is consistent with the typical post-fertilization evolution of mineral N, where NH_4^+ availability peaks and is subsequently depleted as it is oxidized to NO_3^- (Pérez et al., 2001). At our site, the overall dominance of denitrification-related pathways likely reflects poor soil drainage (only 10% sand) and persistently high topsoil (0.05 m) WFPS levels (above 65% during the fertilization in March). Such

https://doi.org/10.5194/egusphere-2026-27
Preprint. Discussion started: 20 January 2026

conditions can create anaerobic environments that favor denitrification (Bateman and Baggs, 2005; Davidson, 1991). The initially low fraction (~0.5) of reduced N_2O following fertilization might be related to elevated NO_3^- concentrations, resulting in NO_2^- accumulation and inhibition of the final reduction step of N_2O to N_2 (Blackmer and Bremner, 1978; Senbayram et al., 2019). Over time, the fraction of reduced N_2O increased markedly, reaching high values on 17 March (~0.8), coincident with topsoil WFPS exceeding 80% and thus favoring complete denitrification. Detailed soil microbial community analyses would be needed to disentangle these competing N_2O production processes, preferentially across different sites and crop rotations.

4.4 Implications for N_2O mitigation in cropland

Our findings reinforce recent studies emphasizing the critical role of vegetation as a N sink in reducing the risk of N_2O emissions from agricultural ecosystems (Feigenwinter et al., 2023; Maier et al., 2022, 2025; Tallec et al., 2022; Timilsina et al., 2024). Specifically, we identified crop establishment and early spring as two phases particularly prone to high N_2O losses during the winter wheat season. These periods were characterized by a mismatch between N supply and plant demand, driven by limited crop growth and substantial mineral N inputs from mineralization or early fertilization, resulting in surplus mineral N in the soil. This excess N, combined with favorable moisture and temperature conditions, created optimal conditions for microbial N_2O production. Stable isotope data further suggested that although denitrification was the dominant process for N_2O production, high mineral N concentrations not only provided the substrates for N_2O production but may also have inhibited the complete reduction of NO_3^- to N_2, thereby increasing the proportion of N lost as N_2O instead of N_2 (Pan et al., 2022). To address these vulnerabilities, management strategies that promote rapid and sustained crop growth, such as optimized sowing dates and cultivar choice, are key N_2O mitigation strategies during the crop establishment phase (Tallec et al., 2022; Maier et al., 2025). In early spring, mitigation will depend on better synchronizing fertilizer N inputs with crop N demand and soil N release. This can be achieved by adjusting both the timing and the amount of N application (Hoben et al., 2011; Omonode et al., 2017), including split applications, site-specific fertilization planning (Jordan-Meille et al., 2023), precision fertilization (Diacono et al., 2013), and enhanced-efficiency fertilizers that slow N release (Akiyama et al., 2010). Finally, site-specific soil conditions should be considered, as they can substantially influence N_2O emission dynamics. At our poorly drained site, elevated soil moisture likely amplified denitrification losses by creating anaerobic conditions. Improving drainage in such settings may therefore help to mitigate N_2O emissions by reducing the extent and duration of these favorable conditions for denitrification (Bouwman, 1996; Grossel et al., 2016).

5.5 Conclusions

The SHAP-based approach proved to be an effective tool for identifying critical periods for N_2O losses and the main drivers for each period. This provided valuable insights into the temporal dynamics of N_2O emissions during a winter wheat cropping season and the subsequent summer cover crop. Thanks to its flexibility and data-driven nature, this method could

https://doi.org/10.5194/egusphere-2026-27
Preprint. Discussion started: 20 January 2026

be applied to other cropping systems to improve understanding of N_2O emission dynamics and inform targeted management. Crop establishment and early spring emerged as particularly vulnerable phases for N_2O losses, largely due to a mismatch between N supply and plant demand. This mismatch, often driven by slow early crop development or early fertilization, led to elevated mineral N levels in the soil, which, under favorable moisture and temperature conditions, created hotspots for microbial N_2O production, primarily through denitrification and/or nitrifier denitrification. Gross primary productivity (GPP), as a proxy for plant N uptake, showed a strong negative relationship with N_2O fluxes, emphasizing the role of active vegetation in limiting emissions. The emission factor (EF) estimated for winter wheat was 1.8%, exceeding IPCC default values, and cumulative N_2O emissions were substantially higher than those previously reported for wheat. These losses notably offset 70% of the climate benefit from net CO_2 uptake, highlighting the need for high-resolution N_2O flux measurements over cropland to accurately represent N_2O emissions in cropland GHG models at regional and global scales. Overall, our findings underscore the importance of implementing management strategies that enhance crop growth in the establishment phase and better align N inputs with plant N demand to reduce N_2O emissions and minimize the GHG footprint of crop production.

Appendix A

Table A1. Management activities conducted during the 2022-2023 measurement period at the cropland in Oensingen.

Crop	Management activity	Date
Grass-clover	Harvest	20 September 2022
	Herbicide application (Glyphosate, W-5553 Sintagro)	3 October 2022
Winter wheat	Sowing (direct seeding)	6 October 2022
	Insecticide application (Sprinter, Netzmittel, Pixxarro)	12 October 2022
	Ammonium nitrate application (Mg-Ammonsalpeter, Landor)	27 February 2023
	Slurry application (dairy)	28 February 2023
	Herbicide application (Concert SX, Derux, Gondor)	22 March 2023
	Ammonium nitrate application (Mg-Ammonsalpeter, Landor)	6 April 2023
	Harvest (grain and straw)	15 July 2023
Bare soil	Soil cultivation (10 cm depth)	17 July 2023
Cover crop	Sowing	27 July 2023
	Mulching	25 September 2023

https://doi.org/10.5194/egusphere-2026-27
Preprint. Discussion started: 20 January 2026

Bare soil	Soil cultivation (10 cm depth)	27 September 2023

Table A2. Overview of key phenological stages of winter wheat, showing the observation dates and corresponding BBCH growth stage numbers during the 2022-23 growing season.

Date	BBCH
11 November 2022	13
22 December 2022	21
7 February 2023	22-23
17 March 2023	24-25
4 April 2023	31
5 May 2023	33
19 May 2023	39
31 May 2023	59
19 June 2023	73
28 June 2023	75
11 July 2023	92

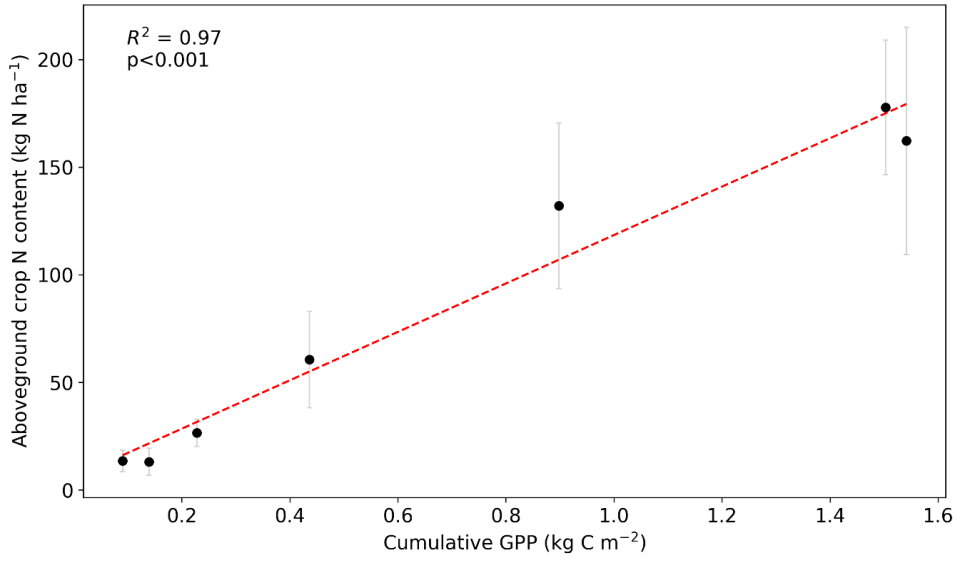

Figure A1. Relationship between cumulative gross primary productivity (GPP) and aboveground crop N content during the wheat growing season. Means ± 1 standard deviation are given (n=12). The dashed red line indicates a linear least-squares regression, with the coefficient of determination (R^2) and respective p-value shown.

https://doi.org/10.5194/egusphere-2026-27
Preprint. Discussion started: 20 January 2026

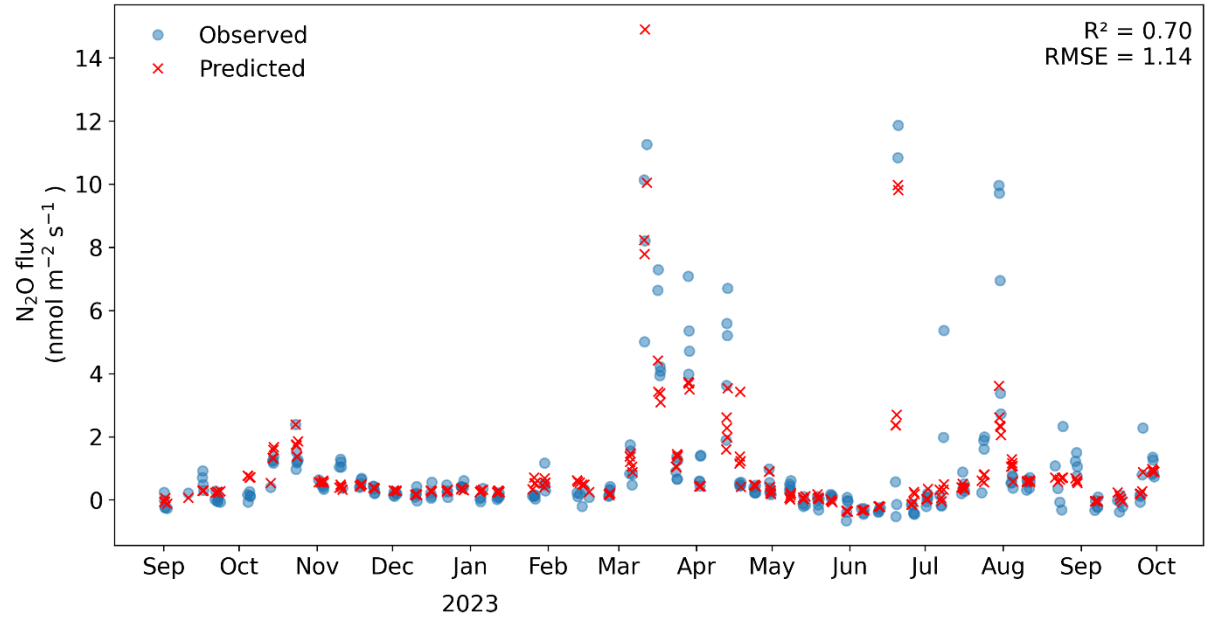

Figure A2. Observed and predicted N_2O fluxes at the cropland Oensingen for the test set (20% of total data). The blue circles represent the values predicted by the XGBoost model, while the red crosses indicate the observed values. The coefficient of determination (R^2) and root mean square error (RMSE) for the test set are given.

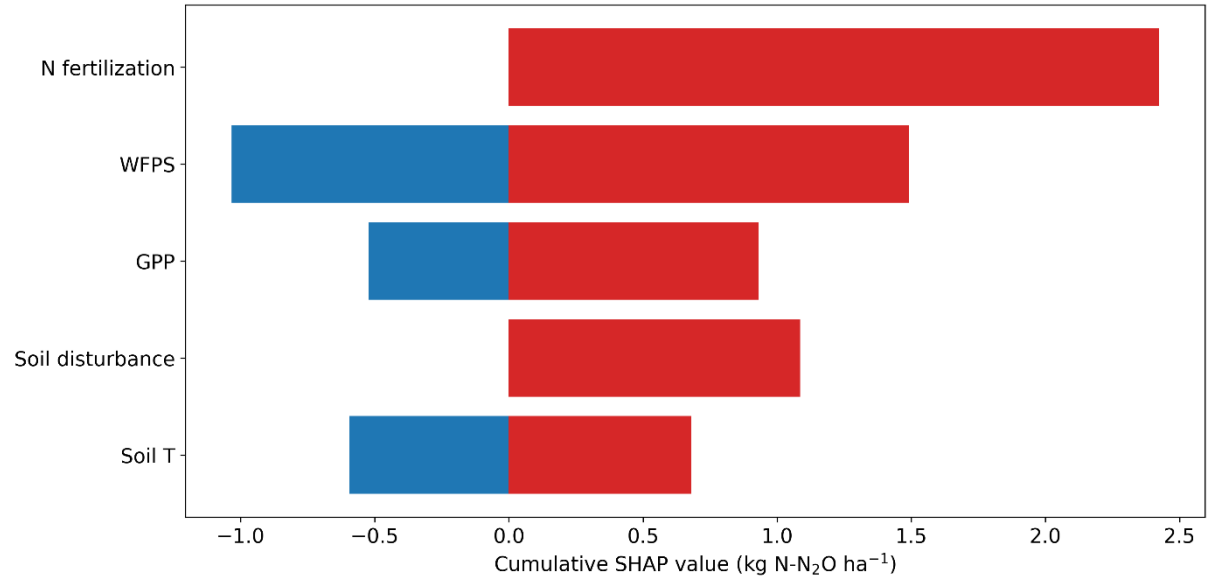

Figure A3. Cumulative positive (red) and negative (blue) SHAP contributions of each driver to predicted N_2O fluxes from September 2022 to October 2023 at the cropland Oensingen. Positive and negative SHAP values were summed up separately, such that increases and decreases in N_2O fluxes are shown independently rather than canceling each other out.

https://doi.org/10.5194/egusphere-2026-27
Preprint. Discussion started: 20 January 2026

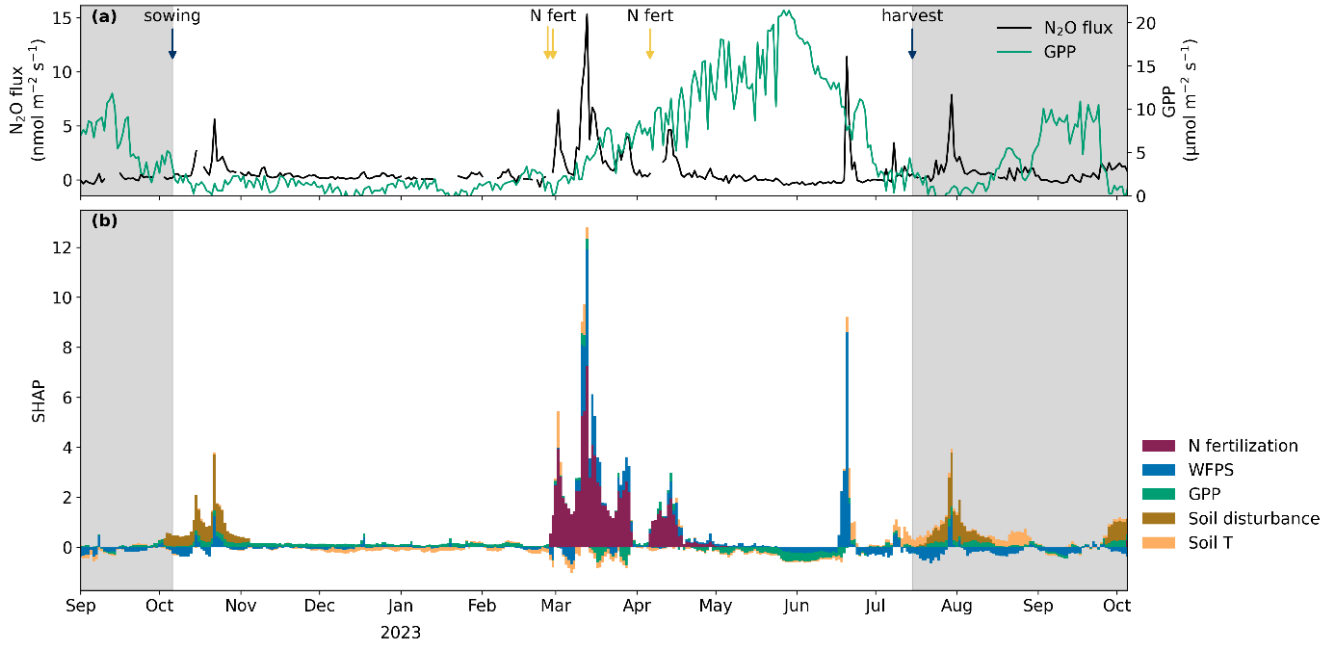

Figure A4. Temporal dynamics of N_2O fluxes, gross primary productivity (GPP), and driver contributions to N_2O fluxes at the Oensingen cropland from September 2022 to October 2023. The unshaded area corresponds to the winter wheat cropping season, while the shaded areas indicate the final phase of the preceding temporary grassland and the cover crop following winter harvest. (a) Daily average N_2O fluxes (measured, highest quality fluxes only) are shown in black, and daily average GPP in green. Arrows at the top denote management activities conducted during the winter wheat cropping season. (b) Contributions of individual drivers (i.e., N fertilization, water-filled pore space (WFPS), GPP, soil disturbance, and soil temperature (soil T)) are expressed as daily averages of SHAP values (see Sect. 2.6.2 for methodological details). The baseline (SHAP = 0) corresponds to a predicted N_2O flux of 0.27 nmol m^{-2} s^{-1}. Positive values indicate a driver's increasing effect on N_2O fluxes, while negative values reflect a decreasing effect.

https://doi.org/10.5194/egusphere-2026-27
Preprint. Discussion started: 20 January 2026

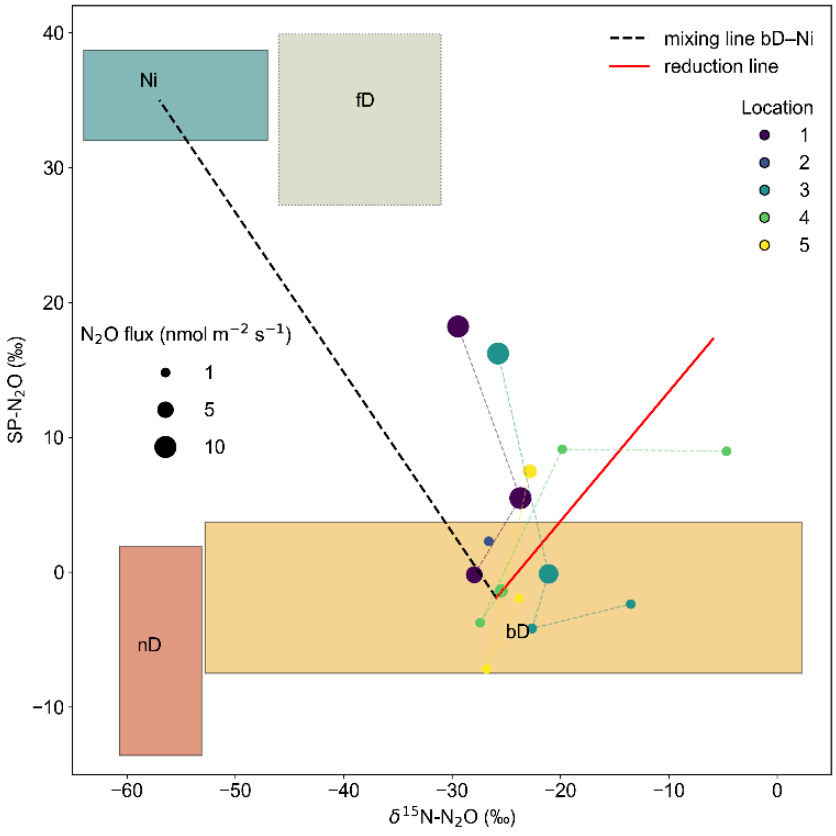

Figure A5. Dual isotope plot of $\delta^{15}N^{bulk}$-N_2O vs. site preference (SP). Colored boxes denote N_2O mixing endmembers (nD: nitrifier denitrification, bD: bacterial denitrification, Ni: nitrification, fD: fungal denitrification). Endmember values are derived from (Yu et al., 2020). Lines for mixing (black) and N_2O reduction to N_2 (red) are shown. Individual measurements are shown as circles, with size reflecting flux magnitude and color indicating location (1 to 5; see Fig. 1).

Code availability

The Python scripts used for data analysis and visualization are available on GitHub (fabioturc/n2o-wheat-drivers-sources) and archived on Zenodo (https://doi.org/10.5281/zenodo.18075225). Scripts used to produce the fluxes dataset are available on GitHub (fabioturc/dataset_ch-oe2_2021-23_flux_product) and Zenodo (https://doi.org/10.5281/zenodo.17975468).

Data availability

Eddy covariance ecosystem fluxes, meteorological data, and management information are openly available for download in the ETH Zurich Research Collection (https://doi.org/10.3929/ethz-c-000782868). All analysis data for this study are also openly available at Zenodo (https://doi.org/10.5281/zenodo.18075225).

https://doi.org/10.5194/egusphere-2026-27
Preprint. Discussion started: 20 January 2026

Author contributions

FT, IF, LA, FL, and NB: conceptualization of the study. FT and LH: data curation. FT: formal analysis, visualization, and writing (original draft preparation). IF, FL, and NB: supervision. FL and NB: project administration. FL and NB: funding acquisition. All authors: methodology and writing (reviewing and editing).

Competing interests

The authors declare that they have no conflict of interest.

Acknowledgements

We gratefully acknowledge the technical assistance of Thomas Baur, Martin Rüegg, Philip Meier, Markus Staudinger, and Peter Ravelhofer for the maintenance of the eddy covariance station at Oensingen. Special thanks go to Matti Barthel for his support in planning the isotope campaign and conducting the N_2O isotope analyses and to Francesco Argento for organizing the Nmin sampling. We also thank Seraina Wagner and Alena Pavlačková for their help in the field and laboratory. Appreciation is extended to Annika Ackermann and Roland A. Werner for running the Stable Isotope Laboratory of the Grassland Sciences Group, as well as to Samuel Tschumi and his team for managing the agricultural field surrounding the flux station. We thank Regine Maier for her guidance on station maintenance and flux processing. We also thank Eliza Harris and Yu Zhou for their valuable advice on the machine-learning model setup. AI tools (ChatGPT, Microsoft Copilot, Grammarly, Consensus, and DeepL) were used to support code development and scientific writing. All AI-assisted content was critically reviewed and revised by the authors to ensure accuracy, clarity, and scientific integrity.

Financial support

We acknowledge funding for the DONA project provided by Nestlé through the ETH Zürich Foundation and the World Food System Center.

References

Akiyama, H., Yan, X., and Yagi, K.: Evaluation of effectiveness of enhanced-efficiency fertilizers as mitigation options for N_2O and NO emissions from agricultural soils: meta-analysis, Glob. Change Biol., 16, 1837–1846, https://doi.org/10.1111/j.1365-2486.2009.02031.x, 2010.

Alaoui, A. and Goetz, B.: Dye tracer and infiltration experiments to investigate macropore flow, Geoderma, 144, 279–286, https://doi.org/10.1016/j.geoderma.2007.11.020, 2008.

https://doi.org/10.5194/egusphere-2026-27
Preprint. Discussion started: 20 January 2026

Ammann, C., Flechard, C. R., Leifeld, J., Neftel, A., and Fuhrer, J.: The carbon budget of newly established temperate grassland depends on management intensity, Agric. Ecosyst. Environ., 121, 5–20, https://doi.org/10.1016/j.agee.2006.12.002, 2007.

Argento, F., Liebisch, F., Simmler, M., Ringger, C., Hatt, M., Walter, A., and Anken, T.: Linking soil N dynamics and plant N uptake by means of sensor support, Eur. J. Agron., 134, 126462, https://doi.org/10.1016/j.eja.2022.126462, 2022.

Aubinet, M., Chermanne, B., Vandenhaute, M., Longdoz, B., Yernaux, M., and Laitat, E.: Long term carbon dioxide exchange above a mixed forest in the Belgian Ardennes, Agric. For. Meteorol., 108, 293–315, https://doi.org/10.1016/S0168-1923(01)00244-1, 2001.

Aubinet, M., Vesala, T., and Papale, D. (Eds.): Eddy covariance: a practical guide to measurement and data analysis, Springer Netherlands, Dordrecht, https://doi.org/10.1007/978-94-007-2351-1, 2012.

Baldocchi, D. D.: Assessing the eddy covariance technique for evaluating carbon dioxide exchange rates of ecosystems: past, present and future, Glob. Change Biol., 9, 479–492, https://doi.org/10.1046/j.1365-2486.2003.00629.x, 2003.

Bateman, E. J. and Baggs, E. M.: Contributions of nitrification and denitrification to N_2O emissions from soils at different water-filled pore space, Biol. Fertil. Soils, 41, 379–388, https://doi.org/10.1007/s00374-005-0858-3, 2005.

Blackmer, A. M. and Bremner, J. M.: Inhibitory effect of nitrate on reduction of N_2O to N_2 by soil microorganisms, Soil Biol. Biochem., 10, 187–191, https://doi.org/10.1016/0038-0717(78)90095-0, 1978.

Bouwman, A. F.: Direct emission of nitrous oxide from agricultural soils, Nutr. Cycl. Agroecosystems, 46, 53–70, https://doi.org/10.1007/BF00210224, 1996.

Breiman, L.: Random forests, Mach. Learn., 45, 5–32, https://doi.org/10.1023/A:1010933404324, 2001.

Buchen, C., Well, R., Helfrich, M., Fuß, R., Kayser, M., Gensior, A., Benke, M., and Flessa, H.: Soil mineral N dynamics and N_2O emissions following grassland renewal, Agric. Ecosyst. Environ., 246, 325–342, https://doi.org/10.1016/j.agee.2017.06.013, 2017.

Buchen, C., Lewicka-Szczebak, D., Flessa, H., and Well, R.: Estimating N_2O processes during grassland renewal and grassland conversion to maize cropping using N_2O isotopocules, Rapid Commun. Mass Spectrom., 32, 1053–1067, https://doi.org/10.1002/rcm.8132, 2018.

Buerge, D.: Die Nmin bestimmung: probenahme, aufbereitung, extraktion und NO_3^- und NH_4^+ messung sowie berechnung. Schweizerische referenzmethoden der forschungsanstalten. Version 1.2, 2020.

Butterbach-Bahl, K., Baggs, E. M., Dannenmann, M., Kiese, R., and Zechmeister-Boltenstern, S.: Nitrous oxide emissions from soils: how well do we understand the processes and their controls?, Philos. Trans. R. Soc. B Biol. Sci., 368, 20130122, 2013.

Carlson, K. M., Gerber, J. S., Mueller, N. D., Herrero, M., MacDonald, G. K., Brauman, K. A., Havlik, P., O'Connell, C. S., Johnson, J. A., Saatchi, S., and West, P. C.: Greenhouse gas emissions intensity of global croplands, Nat. Clim. Change, 7, 63–68, https://doi.org/10.1038/nclimate3158, 2017.

Chatskikh, D. and Olesen, J. E.: Soil tillage enhanced CO_2 and N_2O emissions from loamy sand soil under spring barley, Soil Tillage Res., 97, 5–18, https://doi.org/10.1016/j.still.2007.08.004, 2007.

https://doi.org/10.5194/egusphere-2026-27
Preprint. Discussion started: 20 January 2026

Chen, T. and Guestrin, C.: Xgboost: a scalable tree boosting system, in: Proceedings of the 22nd ACM SIGKDD International Conference on Knowledge Discovery and Data Mining, New York, NY, USA, 785–794, https://doi.org/10.1145/2939672.2939785, 2016.

Ciais, P., Wattenbach, M., Vuichard, N., Smith, P., Piao, S. L., Don, A., Luyssaert, S., Janssens, I. A., Bondeau, A., Dechow, R., Leip, A., Smith, Pc., Beer, C., Van Der Werf, G. R., Gervois, S., Van Oost, K., Tomelleri, E., Freibauer, A., Schulze, E. D., and Team, C. S.: The European carbon balance. Part 2: croplands, Glob. Change Biol., 16, 1409–1428, https://doi.org/10.1111/j.1365-2486.2009.02055.x, 2010.

Davidson, E. A.: Fluxes of nitrous oxide and nitric oxide from terrestrial ecosystems, in: Microbial production and consumption of greenhouse gases: methane, nitrogen oxide, and halomethanes, edited by: Rogers, J. E. and Whitman, W. B., ASM Press, Washington, D.C., 219–235, 1991.

Decock, C. and Six, J.: How reliable is the intramolecular distribution of ^{15}N in N_2O to source partition N_2O emitted from soil?, Soil Biol. Biochem., 65, 114–127, https://doi.org/10.1016/j.soilbio.2013.05.012, 2013.

Del Grosso, S. J., Smith, W., Kraus, D., Massad, R. S., Vogeler, I., and Fuchs, K.: Approaches and concepts of modelling denitrification: increased process understanding using observational data can reduce uncertainties, Curr. Opin. Environ. Sustain., 47, 37–45, https://doi.org/10.1016/j.cosust.2020.07.003, 2020.

Diacono, M., Rubino, P., and Montemurro, F.: Precision nitrogen management of wheat. A review, Agron. Sustain. Dev., 33, 219–241, https://doi.org/10.1007/s13593-012-0111-z, 2013.

Ehleringer, J. R. and Osmond, C. B.: Stable isotopes, in: Plant Physiological Ecology: Field methods and instrumentation, edited by: Pearcy, R. W., Ehleringer, J. R., Mooney, H. A., and Rundel, P. W., Springer Netherlands, Dordrecht, 281–300, https://doi.org/10.1007/978-94-010-9013-1_13, 2000.

Emmel, C., Winkler, A., Hörtnagl, L., Revill, A., Ammann, C., D'Odorico, P., Buchmann, N., and Eugster, W.: Integrated management of a Swiss cropland is not sufficient to preserve its soil carbon pool in the long term, Biogeosciences, 15, 5377–5393, https://doi.org/10.5194/bg-15-5377-2018, 2018.

Epper, C. A., Zavattaro, L., Velthof, G. L., Thuriès, L., Steinsberger, T., Sørensen, P., Richards, K., Oberson, A., Möller, K., Merbold, L., Menzi, H., Liebisch, F., Levavasseur, F., Leiber, F., Kupper, T., Krol, D., Janke, D., Hofmeier, M., Hoekstra, N. J., Guillaume, T., Gilgen, A., Ghiasi, S., Frick, H., Dragoni, F., Otálora, X. D. de, Chadwick, D. R., Cavalli, D., Bretscher, D., Bischoff, W.-A., Bechini, L., Argento, F., Amon, B., Ammann, C., and Mayer, J.: Chapter Six - Optimizing nitrogen use efficiency in European livestock systems: from feed to plant growth, vol. 191, edited by: Sparks, D. L., Academic Press, 277–362, https://doi.org/10.1016/bs.agron.2025.01.003, 2025.

Erisman, J. W., Sutton, M. A., Galloway, J., Klimont, Z., and Winiwarter, W.: How a century of ammonia synthesis changed the world, Nat. Geosci., 1, 636–639, https://doi.org/10.1038/ngeo325, 2008.

European Commission: Council Directive 91/676/EEC of 12 December 1991 concerning the protection of waters against pollution caused by nitrates from agricultural sources, 1991.

Feigenwinter, I., Hörtnagl, L., and Buchmann, N.: N_2O and CH_4 fluxes from intensively managed grassland: the importance of biological and environmental drivers vs. management, Sci. Total Environ., 903, 166389, https://doi.org/10.1016/j.scitotenv.2023.166389, 2023.

FOEN: Switzerland's greenhouse gas inventory 1990–2023: national inventory document and reporting tables (CRT). Submission of 2025 under the United Nations framework convention on climate change and under the Paris agreement., Federal Office for the Environment, Bern, 2025.

Forster, P., Storelvmo, T., Armour, K., Collins, W., Dufresne, J.-L., Frame, D., Lunt, D. J., Mauritsen, T., Palmer, M. D., Watanabe, M., Wild, M., and Zhang, H.: The Earth's energy budget, climate feedbacks, and climate sensitivity, in: Climate change 2021: the physical science basis. Contribution of working group I to the sixth assessment report of the intergovernmental panel on climate change, edited by: Masson-Delmotte, V., Zhai, P., Pirani, A., Connors, S. L., Péan, C., Berger, S., Caud, N., Chen, Y., Goldfarb, L., Gomis, M. I., Huang, M., Leitzell, K., Lonnoy, E., Matthews, J. B. R., Maycock, T. K., Waterfield, T., Yelekçi, O., Yu, R., and Zhou, B., Cambridge University Press, Cambridge, United Kingdom and New York, NY, USA, 923–1054, https://doi.org/10.1017/9781009157896.009, 2021.

Fratini, G., Ibrom, A., Arriga, N., Burba, G., and Papale, D.: Relative humidity effects on water vapour fluxes measured with closed-path eddy-covariance systems with short sampling lines, Agric. For. Meteorol., 165, 53–63, https://doi.org/10.1016/j.agrformet.2012.05.018, 2012.

Gallarotti, N., Barthel, M., Verhoeven, E., Pereira, E. I. P., Bauters, M., Baumgartner, S., Drake, T. W., Boeckx, P., Mohn, J., Longepierre, M., Mugula, J. K., Makelele, I. A., Ntaboba, L. C., and Six, J.: In-depth analysis of N_2O fluxes in tropical forest soils of the Congo Basin combining isotope and functional gene analysis, ISME J., 15, 3357–3374, https://doi.org/10.1038/s41396-021-01004-x, 2021.

Garnier, J., Casquin, A., Mercier, B., Martinez, A., Gréhan, E., Azougui, A., Bosc, S., Pomet, A., Billen, G., and Mary, B.: Six years of nitrous oxide emissions from temperate cropping systems under real-farm rotational management, Agric. For. Meteorol., 354, 110085, https://doi.org/10.1016/j.agrformet.2024.110085, 2024.

Gnisia, G., Weik, J., Ruser, R., Essich, L., Lewandowski, I., and Stein, A.: Machine learning-based prediction of nitrous oxide emissions from arable farming: exploring management practices as predictor variables, Ecol. Indic., 172, 113233, https://doi.org/10.1016/j.ecolind.2025.113233, 2025.

Goodrich, J. P., Wall, A. M., Campbell, D. I., Fletcher, D., Wecking, A. R., and Schipper, L. A.: Improved gap filling approach and uncertainty estimation for eddy covariance N_2O fluxes, Agric. For. Meteorol., 297, 108280, https://doi.org/10.1016/j.agrformet.2020.108280, 2021.

Grandy, A. S. and Robertson, G. P.: Initial cultivation of a temperate-region soil immediately accelerates aggregate turnover and CO_2 and N_2O fluxes, Glob. Change Biol., 12, 1507–1520, https://doi.org/10.1111/j.1365-2486.2006.01166.x, 2006.

Grossel, A., Nicoullaud, B., Bourennane, H., Lacoste, M., Guimbaud, C., Robert, C., and Hénault, C.: The effect of tile-drainage on nitrous oxide emissions from soils and drainage streams in a cropped landscape in Central France, Agric. Ecosyst. Environ., 230, 251–260, https://doi.org/10.1016/j.agee.2016.06.015, 2016.

Guyon, I., Weston, J., Barnhill, S., and Vapnik, V.: Gene selection for cancer classification using support vector machines, Mach. Learn., 46, 389–422, https://doi.org/10.1023/A:1012487302797, 2002.

Hamrani, A., Akbarzadeh, A., and Madramootoo, C. A.: Machine learning for predicting greenhouse gas emissions from agricultural soils, Sci. Total Environ., 741, 140338, https://doi.org/10.1016/j.scitotenv.2020.140338, 2020.

Harris, C. R., Millman, K. J., van der Walt, S. J., Gommers, R., Virtanen, P., Cournapeau, D., Wieser, E., Taylor, J., Berg, S., Smith, N. J., Kern, R., Picus, M., Hoyer, S., van Kerkwijk, M. H., Brett, M., Haldane, A., del Río, J. F., Wiebe, M., Peterson, P., Gérard-Marchant, P., Sheppard, K., Reddy, T., Weckesser, W., Abbasi, H., Gohlke, C., and Oliphant, T. E.: Array programming with NumPy, Nature, 585, 357–362, https://doi.org/10.1038/s41586-020-2649-2, 2020a.

https://doi.org/10.5194/egusphere-2026-27
Preprint. Discussion started: 20 January 2026

Harris, S. J., Liisberg, J., Xia, L., Wei, J., Zeyer, K., Yu, L., Barthel, M., Wolf, B., Kelly, B. F. J., Cendón, D. I., Blunier, T., Six, J., and Mohn, J.: N_2O isotopocule measurements using laser spectroscopy: analyzer characterization and intercomparison, Atmospheric Meas. Tech., 13, 2797–2831, https://doi.org/10.5194/amt-13-2797-2020, 2020b.

Helfrich, M., Nicolay, G., Well, R., Buchen-Tschiskale, C., Dechow, R., Fuß, R., Gensior, A., Paulsen, H. M., Berendonk, C., and Flessa, H.: Effect of chemical and mechanical grassland conversion to cropland on soil mineral N dynamics and N_2O emission, Agric. Ecosyst. Environ., 298, 106975, https://doi.org/10.1016/j.agee.2020.106975, 2020.

Hoben, J. P., Gehl, R. J., Millar, N., Grace, P. R., and Robertson, G. P.: Nonlinear nitrous oxide (N_2O) response to nitrogen fertilizer in on-farm corn crops of the US Midwest, Glob. Change Biol., 17, 1140–1152, https://doi.org/10.1111/j.1365-2486.2010.02349.x, 2011.

Horst, T. W. and Lenschow, D. H.: Attenuation of scalar fluxes measured with spatially-displaced sensors, Bound.-Layer Meteorol., 130, 275–300, https://doi.org/10.1007/s10546-008-9348-0, 2009.

Hörtnagl, L.: diive, https://doi.org/10.5281/zenodo.16386810, 2025.

Hörtnagl, L., Barthel, M., Buchmann, N., Eugster, W., Butterbach-Bahl, K., Díaz-Pinés, E., Zeeman, M., Klumpp, K., Kiese, R., Bahn, M., Hammerle, A., Lu, H., Ladreiter-Knauss, T., Burri, S., and Merbold, L.: Greenhouse gas fluxes over managed grasslands in Central Europe, Glob. Change Biol., 24, 1843–1872, https://doi.org/10.1111/gcb.14079, 2018.

Hunter, J. D.: Matplotlib: A 2D graphics environment, Comput. Sci. Eng., 9, 90–95, https://doi.org/10.1109/MCSE.2007.55, 2007.

IPCC: N_2O emissions from managed soils, and CO_2 emissions from lime and urea application, Chapter 11, in: 2019 refinement to the 2006 IPCC guidelines for national greenhouse gas inventories, edited by: Calvo Buendia, E., Tanabe, K., Kranjc, A., Baasansuren, J., Fukuda, M., Ngarize, S., Osako, A., Pyrozhenko, Y., Shermanau, P., and Federici, S., Intergovernmental Panel on Climate Change (IPCC), Geneva, Switzerland, 2019.

IPCC: Climate change 2021 - the physical science basis: contribution of working group I to the sixth assessment report of the intergovernmental panel on climate change, Cambridge University Press, 2021.

Jordan-Meille, L., Denoroy, P., Dittert, K., Cugnon, T., Quemada, M., Wall, D., Bechini, L., Marx, S., Oenema, O., Reijneveld, A., Liebisch, F., Diedhiou, K., Degan, F., and Higgins, S.: Comparison of nitrogen fertilisation recommendations of West European Countries, Eur. J. Soil Sci., 74, e13436, https://doi.org/10.1111/ejss.13436, 2023.

Kljun, N., Calanca, P., Rotach, M. W., and Schmid, H. P.: A simple two-dimensional parameterisation for Flux Footprint Prediction (FFP), Geosci. Model Dev., 8, 3695–3713, https://doi.org/10.5194/gmd-8-3695-2015, 2015.

Krebs, L., Hörtnagl, L., Scapucci, L., Gharun, M., Feigenwinter, I., and Buchmann, N.: Net ecosystem CO_2 exchange of a subalpine spruce forest in Switzerland over 26 years: effects of phenology and contributions of abiotic drivers at daily time scales, Glob. Change Biol., 31, e70371, https://doi.org/10.1111/gcb.70371, 2025.

Ladha, J. K., Pathak, H., J. Krupnik, T., Six, J., and van Kessel, C.: Efficiency of fertilizer nitrogen in cereal production: retrospects and prospects, in: Advances in Agronomy, vol. 87, Academic Press, 85–156, https://doi.org/10.1016/S0065-2113(05)87003-8, 2005.

Lassaletta, L., Billen, G., Grizzetti, B., Anglade, J., and Garnier, J.: 50 year trends in nitrogen use efficiency of world cropping systems: the relationship between yield and nitrogen input to cropland, Environ. Res. Lett., 9, 105011, https://doi.org/10.1088/1748-9326/9/10/105011, 2014.

https://doi.org/10.5194/egusphere-2026-27
Preprint. Discussion started: 20 January 2026

Le Mer, J. and Roger, P.: Production, oxidation, emission and consumption of methane by soils: a review, Eur. J. Soil Biol., 37, 25–50, https://doi.org/10.1016/S1164-5563(01)01067-6, 2001.

Lewicka-Szczebak, D., Lewicki, M. P., and Well, R.: N_2O isotope approaches for source partitioning of N_2O production and estimation of N_2O reduction – validation with the ^{15}N gas-flux method in laboratory and field studies, Biogeosciences, 17, 5513–5537, https://doi.org/10.5194/bg-17-5513-2020, 2020.

Lewicki, M. P., Lewicka-Szczebak, D., and Skrzypek, G.: FRAME—Monte Carlo model for evaluation of the stable isotope mixing and fractionation, PLOS ONE, 17, e0277204, https://doi.org/10.1371/journal.pone.0277204, 2022.

Liang, G.: Nitrogen fertilization mitigates global food insecurity by increasing cereal yield and its stability, Glob. Food Secur., 34, 100652, https://doi.org/10.1016/j.gfs.2022.100652, 2022.

Lognoul, M., Debacq, A., De Ligne, A., Dumont, B., Manise, T., Bodson, B., Heinesch, B., and Aubinet, M.: N_2O flux short-term response to temperature and topsoil disturbance in a fertilized crop: an eddy covariance campaign, Agric. For. Meteorol., 271, 193–206, https://doi.org/10.1016/j.agrformet.2019.02.033, 2019.

Lundberg, S. M. and Lee, S.-I.: A unified approach to interpreting model predictions, in: Advances in neural information processing systems, 30, 2017.

Lundberg, S. M., Erion, G., Chen, H., DeGrave, A., Prutkin, J. M., Nair, B., Katz, R., Himmelfarb, J., Bansal, N., and Lee, S.-I.: From local explanations to global understanding with explainable AI for trees, Nat. Mach. Intell., 2, 56–67, https://doi.org/10.1038/s42256-019-0138-9, 2020.

Maier, R., Hörtnagl, L., and Buchmann, N.: Greenhouse gas fluxes (CO_2, N_2O and CH_4) of pea and maize during two cropping seasons: drivers, budgets, and emission factors for nitrous oxide, Sci. Total Environ., 849, 157541, https://doi.org/10.1016/j.scitotenv.2022.157541, 2022.

Maier, R., Hörtnagl, L., and Buchmann, N.: Large nitrous oxide emissions from arable soils after crop harvests prior to sowing, Nutr. Cycl. Agroecosystems, https://doi.org/10.1007/s10705-024-10395-0, 2025.

Mauder, M. and Foken, T.: Documentation and instruction manual of the eddy covariance software package TK2, University of Bayreuth, Department of Micrometeorology, Bayreuth, Germany, 2004.

McKinney, W.: Data structures for statistical computing in Python, in: Proceedings of the 9th Python in Science Conference, 56–61, https://doi.org/10.25080/Majora-92bf1922-00a, 2010.

Meier, U.: Growth stages of mono- and dicotyledonous plants: BBCH Monograph, https://doi.org/10.5073/20180906-074619, 2018.

Merbold, L., Eugster, W., Stieger, J., Zahniser, M., Nelson, D., and Buchmann, N.: Greenhouse gas budget (CO_2, CH_4 and N_2O) of intensively managed grassland following restoration, Glob. Change Biol., 20, 1913–1928, https://doi.org/10.1111/gcb.12518, 2014.

Molnar, C.: Interpretable machine learning: a guide for making black box models explainable, 3rd ed., 2025.

Moncrieff, J., Clement, R., Finnigan, J., and Meyers, T.: Averaging, detrending, and filtering of eddy covariance time series, in: Handbook of micrometeorology: a guide for surface flux measurement and analysis, edited by: Lee, X., Massman, W., and Law, B., Springer Netherlands, Dordrecht, 7–31, https://doi.org/10.1007/1-4020-2265-4_2, 2005.

https://doi.org/10.5194/egusphere-2026-27
Preprint. Discussion started: 20 January 2026

Nabuurs, G.-J., Mrabet, R., Abu Hatab, A., Bustamante, M., Clark, H., Havlík, P., House, J., Mbow, C., Ninan, K. N., Popp, A., Roe, S., Sohngen, B., and Towprayoon, S.: Agriculture, forestry and other land uses (AFOLU), in: Climate change 2022: mitigation of climate change. Contribution of working group III to the sixth assessment report of the intergovernmental panel on climate change, edited by: Shukla, P. R., Skea, J., Slade, R., Al Khourdajie, A., van Diemen, R., McCollum, D., Pathak, M., Some, S., Vyas, P., Fradera, R., Belkacemi, M., Hasija, A., Lisboa, G., Luz, S., and Malley, J., Cambridge University Press, Cambridge, UK and New York, USA, https://doi.org/10.1017/9781009157926.009, 2022.

Nemitz, E., Mammarella, I., Ibrom, A., Aurela, M., Burba, G. G., Dengel, S., Gielen, B., Grelle, A., Heinesch, B., Herbst, M., Hörtnagl, L., Klemedtsson, L., Lindroth, A., Lohila, A., McDermitt, D. K., Meier, P., Merbold, L., Nelson, D., Nicolini, G., Nilsson, M. B., Peltola, O., Rinne, J., and Zahniser, M.: Standardisation of eddy-covariance flux measurements of methane and nitrous oxide, Int. Agrophysics, 32, 517–549, https://doi.org/10.1515/intag-2017-0042, 2018.

Omonode, R. A., Halvorson, A. D., Gagnon, B., and Vyn, T. J.: Achieving lower nitrogen balance and higher nitrogen recovery efficiency reduces nitrous oxide emissions in North America's maize cropping systems, Front. Plant Sci., 8, https://doi.org/10.3389/fpls.2017.01080, 2017.

Papale, D., Reichstein, M., Aubinet, M., Canfora, E., Bernhofer, C., Kutsch, W., Longdoz, B., Rambal, S., Valentini, R., Vesala, T., and Yakir, D.: Towards a standardized processing of net ecosystem exchange measured with eddy covariance technique: algorithms and uncertainty estimation, Biogeosciences, 3, 571–583, https://doi.org/10.5194/bg-3-571-2006, 2006.

Pastorello, G., Trotta, C., Canfora, E., Chu, H., Christianson, D., Cheah, Y.-W., Poindexter, C., Chen, J., Elbashandy, A., Humphrey, M., Isaac, P., Polidori, D., Reichstein, M., Ribeca, A., van Ingen, C., Vuichard, N., Zhang, L., Amiro, B., Ammann, C., Arain, M. A., Ardö, J., Arkebauer, T., Arndt, S. K., Arriga, N., Aubinet, M., Aurela, M., Baldocchi, D., Barr, A., Beamesderfer, E., Marchesini, L. B., Bergeron, O., Beringer, J., Bernhofer, C., Berveiller, D., Billesbach, D., Black, T. A., Blanken, P. D., Bohrer, G., Boike, J., Bolstad, P. V., Bonal, D., Bonnefond, J.-M., Bowling, D. R., Bracho, R., Brodeur, J., Brümmer, C., Buchmann, N., Burban, B., Burns, S. P., Buysse, P., Cale, P., Cavagna, M., Cellier, P., Chen, S., Chini, I., Christensen, T. R., Cleverly, J., Collalti, A., Consalvo, C., Cook, B. D., Cook, D., Coursolle, C., Cremonese, E., Curtis, P. S., D'Andrea, E., da Rocha, H., Dai, X., Davis, K. J., Cinti, B. D., Grandcourt, A. de, Ligne, A. D., De Oliveira, R. C., Delpierre, N., Desai, A. R., Di Bella, C. M., Tommasi, P. di, Dolman, H., Domingo, F., Dong, G., Dore, S., Duce, P., Dufrêne, E., Dunn, A., Dušek, J., Eamus, D., Eichelmann, U., ElKhidir, H. A. M., Eugster, W., Ewenz, C. M., Ewers, B., Famulari, D., Fares, S., Feigenwinter, I., Feitz, A., Fensholt, R., Filippa, G., Fischer, M., Frank, J., Galvagno, M., et al.: The FLUXNET2015 dataset and the ONEFlux processing pipeline for eddy covariance data, Sci. Data, 7, 225, https://doi.org/10.1038/s41597-020-0534-3, 2020.

Pedregosa, F., Varoquaux, G., Gramfort, A., Michel, V., Thirion, B., Grisel, O., Blondel, M., Prettenhofer, P., Weiss, R., Dubourg, V., Vanderplas, J., Passos, A., Cournapeau, D., Brucher, M., Perrot, M., and Duchesnay, É.: Scikit-learn: machine learning in Python, J Mach Learn Res, 12, 2825–2830, 2011.

Pérez, T., Trumbore, S. E., Tyler, S. C., Matson, P. A., Ortiz-Monasterio, I., Rahn, T., and Griffith, D. W. T.: Identifying the agricultural imprint on the global N_2O budget using stable isotopes, J. Geophys. Res. Atmospheres, 106, 9869–9878, https://doi.org/10.1029/2000JD900809, 2001.

Philibert, A., Loyce, C., and Makowski, D.: Prediction of N_2O emission from local information with Random Forest, Environ. Pollut., 177, 156–163, https://doi.org/10.1016/j.envpol.2013.02.019, 2013.

Portmann, R. W., Daniel, J. S., and Ravishankara, A. R.: Stratospheric ozone depletion due to nitrous oxide: influences of other gases, Philos. Trans. R. Soc. B Biol. Sci., 367, 1256–1264, https://doi.org/10.1098/rstb.2011.0377, 2012.

Ravishankara, A. R., Daniel, J. S., and Portmann, R. W.: Nitrous oxide (N_2O): the dominant ozone-depleting substance emitted in the 21st century, Science, 326, 123–125, https://doi.org/10.1126/science.1176985, 2009.

https://doi.org/10.5194/egusphere-2026-27
Preprint. Discussion started: 20 January 2026

Reichstein, M., Falge, E., Baldocchi, D., Papale, D., Aubinet, M., Berbigier, P., Bernhofer, C., Buchmann, N., Gilmanov, T., Granier, A., Grünwald, T., Havránková, K., Ilvesniemi, H., Janous, D., Knohl, A., Laurila, T., Lohila, A., Loustau, D., Matteucci, G., Meyers, T., Miglietta, F., Ourcival, J.-M., Pumpanen, J., Rambal, S., Rotenberg, E., Sanz, M., Tenhunen, J., Seufert, G., Vaccari, F., Vesala, T., Yakir, D., and Valentini, R.: On the separation of net ecosystem exchange into assimilation and ecosystem respiration: review and improved algorithm, Glob. Change Biol., 11, 1424–1439, https://doi.org/10.1111/j.1365-2486.2005.001002.x, 2005.

Rummel, P. S., Englert, P., Beule, L., and Pausch, J.: N_2O flux dynamics and production pathways modulated by soil organic matter and litter turnover, Biol. Fertil. Soils, https://doi.org/10.1007/s00374-025-01925-1, 2025.

Ruosteenoja, K., Markkanen, T., Venäläinen, A., Räisänen, P., and Peltola, H.: Seasonal soil moisture and drought occurrence in Europe in CMIP5 projections for the 21st century, Clim. Dyn., 50, 1177–1192, https://doi.org/10.1007/s00382-017-3671-4, 2018.

Sabbatini, S., Mammarella, I., Arriga, N., Fratini, G., Graf, A., Hörtnagl, L., Ibrom, A., Longdoz, B., Mauder, M., Merbold, L., Metzger, S., Montagnani, L., Pitacco, A., Rebmann, C., Sedlák, P., Šigut, L., Vitale, D., and Papale, D.: Eddy covariance raw data processing for CO_2 and energy fluxes calculation at ICOS ecosystem stations, Int. Agrophysics, 32, 495–515, https://doi.org/10.1515/intag-2017-0043, 2018.

Saha, D., Basso, B., and Robertson, G. P.: Machine learning improves predictions of agricultural nitrous oxide (N_2O) emissions from intensively managed cropping systems, Environ. Res. Lett., 16, 024004, https://doi.org/10.1088/1748-9326/abd2f3, 2021.

Scapucci, L., Shekhar, A., Aranda-Barranco, S., Bolshakova, A., Hörtnagl, L., Gharun, M., and Buchmann, N.: Compound soil and atmospheric drought (CSAD) events and CO_2 fluxes of a mixed deciduous forest: the occurrence, impact, and temporal contribution of main drivers, Biogeosciences, 21, 3571–3592, https://doi.org/10.5194/bg-21-3571-2024, 2024.

Scapucci, L., Krebs, L., Burri, S., Hörtnagl, L., and Buchmann, N.: Soil and forest floor respiration already acclimated to increasing temperatures in a mixed deciduous forest, Ecol. Process., 14, 71, https://doi.org/10.1186/s13717-025-00639-4, 2025.

Schulze, E. D., Luyssaert, S., Ciais, P., Freibauer, A., Janssens, I. A., Soussana, J. F., Smith, P., Grace, J., Levin, I., Thiruchittampalam, B., Heimann, M., Dolman, A. J., Valentini, R., Bousquet, P., Peylin, P., Peters, W., Rödenbeck, C., Etiope, G., Vuichard, N., Wattenbach, M., Nabuurs, G. J., Poussi, Z., Nieschulze, J., and Gash, J. H.: Importance of methane and nitrous oxide for Europe's terrestrial greenhouse-gas balance, Nat. Geosci., 2, 842–850, https://doi.org/10.1038/ngeo686, 2009.

Senbayram, M., Budai, A., Bol, R., Chadwick, D., Marton, L., Gündogan, R., and Wu, D.: Soil NO_3^- level and O_2 availability are key factors in controlling N_2O reduction to N_2 following long-term liming of an acidic sandy soil, Soil Biol. Biochem., 132, 165–173, https://doi.org/10.1016/j.soilbio.2019.02.009, 2019.

Shang, Z., Cui, X., van Groenigen, K. J., Kuhnert, M., Abdalla, M., Luo, J., Zhang, W., Song, Z., Jiang, Y., Smith, P., and Zhou, F.: Global cropland nitrous oxide emissions in fallow period are comparable to growing-season emissions, Glob. Change Biol., 30, e17165, https://doi.org/10.1111/gcb.17165, 2024.

Shcherbak, I., Millar, N., and Robertson, G. P.: Global meta-analysis of the nonlinear response of soil nitrous oxide (N_2O) emissions to fertilizer nitrogen, Proc. Natl. Acad. Sci., 111, 9199–9204, https://doi.org/10.1073/pnas.1322434111, 2014.

Smith, K. A.: Changing views of nitrous oxide emissions from agricultural soil: key controlling processes and assessment at different spatial scales, Eur. J. Soil Sci., 68, 137–155, https://doi.org/10.1111/ejss.12409, 2017.

https://doi.org/10.5194/egusphere-2026-27
Preprint. Discussion started: 20 January 2026

Smith, K. A., McTaggart, I. P., Dobbie, K. E., and Conen, F.: Emissions of N_2O from Scottish agricultural soils, as a function of fertilizer N, Nutr. Cycl. Agroecosystems, 52, 123–130, https://doi.org/10.1023/A:1009781518738, 1998.

Swiss Federal Council: Water Protection Ordinance (WPO, 814.201) of 28 October 1998, 1998.

Swiss Federal Council: Verordnung über die Direktzahlungen an die Landwirtschaft (Direktzahlungsverordnung, DZV) vom 23. Oktober 2013 (Stand am 1. Januar 2025), 2025.

Tallec, T., Bigaignon, L., Delon, C., Brut, A., Ceschia, E., Mordelet, P., Zawilski, B., Granouillac, F., Claverie, N., Fieuzal, R., Lemaire, B., and Le Dantec, V.: Dynamics of nitrous oxide emissions from two cropping systems in southwestern France over 5 years: cross impact analysis of heterogeneous agricultural practices and local climate variability, Agric. For. Meteorol., 323, 109093, https://doi.org/10.1016/j.agrformet.2022.109093, 2022.

Tian, H., Pan, N., Thompson, R. L., Canadell, J. G., Suntharalingam, P., Regnier, P., Davidson, E. A., Prather, M., Ciais, P., Muntean, M., Pan, S., Winiwarter, W., Zaehle, S., Zhou, F., Jackson, R. B., Bange, H. W., Berthet, S., Bian, Z., Bianchi, D., Bouwman, A. F., Buitenhuis, E. T., Dutton, G., Hu, M., Ito, A., Jain, A. K., Jeltsch-Thömmes, A., Joos, F., Kou-Giesbrecht, S., Krummel, P. B., Lan, X., Landolfi, A., Lauerwald, R., Li, Y., Lu, C., Maavara, T., Manizza, M., Millet, D. B., Mühle, J., Patra, P. K., Peters, G. P., Qin, X., Raymond, P., Resplandy, L., Rosentreter, J. A., Shi, H., Sun, Q., Tonina, D., Tubiello, F. N., van der Werf, G. R., Vuichard, N., Wang, J., Wells, K. C., Western, L. M., Wilson, C., Yang, J., Yao, Y., You, Y., and Zhu, Q.: Global nitrous oxide budget (1980–2020), Earth Syst. Sci. Data, 16, 2543–2604, https://doi.org/10.5194/essd-16-2543-2024, 2024.

Timilsina, A., Neupane, P., Yao, J., Raseduzzaman, M., Bizimana, F., Pandey, B., Feyissa, A., Li, X., Dong, W., Yadav, R. K. P., Gomez-Casanovas, N., and Hu, C.: Plants mitigate ecosystem nitrous oxide emissions primarily through reductions in soil nitrate content: evidence from a meta-analysis, Sci. Total Environ., 949, 175115, https://doi.org/10.1016/j.scitotenv.2024.175115, 2024.

Toyoda, S. and Yoshida, N.: Determination of nitrogen isotopomers of nitrous oxide on a modified isotope ratio mass spectrometer, Anal. Chem., 71, 4711–4718, https://doi.org/10.1021/ac9904563, 1999.

Toyoda, S., Yoshida, N., Miwa, T., Matsui, Y., Yamagishi, H., Tsunogai, U., Nojiri, Y., and Tsurushima, N.: Production mechanism and global budget of N_2O inferred from its isotopomers in the western North Pacific, Geophys. Res. Lett., 29, 7–1, https://doi.org/10.1029/2001GL014311, 2002.

Turco, F.: fabioturc/dataset_ch-oe2_2021-23_flux_product: FP2025.12, https://doi.org/10.5281/zenodo.17975468, 2025a.

Turco, F.: fabioturc/n2o-wheat-drivers-sources: version 2025-12-28, https://doi.org/10.5281/zenodo.18075225, 2025b.

Van Groenigen, J. W., Velthof, G. L., Oenema, O., Van Groenigen, K. J., and Van Kessel, C.: Towards an agronomic assessment of N_2O emissions: a case study for arable crops, Eur. J. Soil Sci., 61, 903–913, https://doi.org/10.1111/j.1365-2389.2009.01217.x, 2010.

Verhoeven, E., Barthel, M., Yu, L., Celi, L., Said-Pullicino, D., Sleutel, S., Lewicka-Szczebak, D., Six, J., and Decock, C.: Early season N_2O emissions under variable water management in rice systems: source-partitioning emissions using isotope ratios along a depth profile, Biogeosciences, 16, 383–408, https://doi.org/10.5194/bg-16-383-2019, 2019.

Vickers, D. and Mahrt, L.: Quality control and flux sampling problems for tower and aircraft data, J. Atmospheric Ocean. Technol., 14, 512–526, https://doi.org/10.1175/1520-0426(1997)014<0512:QCAFSP>2.0.CO;2, 1997.

https://doi.org/10.5194/egusphere-2026-27
Preprint. Discussion started: 20 January 2026

Virtanen, P., Gommers, R., Oliphant, T. E., Haberland, M., Reddy, T., Cournapeau, D., Burovski, E., Peterson, P., Weckesser, W., Bright, J., van der Walt, S. J., Brett, M., Wilson, J., Millman, K. J., Mayorov, N., Nelson, A. R. J., Jones, E., Kern, R., Larson, E., Carey, C. J., Polat, İ., Feng, Y., Moore, E. W., VanderPlas, J., Laxalde, D., Perktold, J., Cimrman, R., Henriksen, I., Quintero, E. A., Harris, C. R., Archibald, A. M., Ribeiro, A. H., Pedregosa, F., and van Mulbregt, P.: SciPy 1.0: fundamental algorithms for scientific computing in Python, Nat. Methods, 17, 261–272, https://doi.org/10.1038/s41592-019-0686-2, 2020.

Waskom, M. L.: Seaborn: statistical data visualization, J. Open Source Softw., 6, 3021, https://doi.org/10.21105/joss.03021, 2021.

Wilczak, J. M., Oncley, S. P., and Stage, S. A.: Sonic anemometer tilt correction algorithms, Bound.-Layer Meteorol., 99, 127–150, https://doi.org/10.1023/A:1018966204465, 2001.

Wutzler, T., Lucas-Moffat, A., Migliavacca, M., Knauer, J., Sickel, K., Šigut, L., Menzer, O., and Reichstein, M.: Basic and extensible post-processing of eddy covariance flux data with REddyProc, Biogeosciences, 15, 5015–5030, https://doi.org/10.5194/bg-15-5015-2018, 2018.

Yao, Z., Guo, H., Wang, Y., Zhan, Y., Zhang, T., Wang, R., Zheng, X., and Butterbach-Bahl, K.: A global meta-analysis of yield-scaled N_2O emissions and its mitigation efforts for maize, wheat, and rice, Glob. Change Biol., 30, e17177, https://doi.org/10.1111/gcb.17177, 2024.

Yu, L., Harris, E., Lewicka-Szczebak, D., Barthel, M., Blomberg, M. R. A., Harris, S. J., Johnson, M. S., Lehmann, M. F., Liisberg, J., Müller, C., Ostrom, N. E., Six, J., Toyoda, S., Yoshida, N., and Mohn, J.: What can we learn from N_2O isotope data? Analytics, processes and modelling, Rapid Commun. Mass Spectrom., 34, https://doi.org/10.1002/rcm.8858, 2020.

Yu, X., Keitel, C., Zhang, Y., Wangeci, A. N., and Dijkstra, F. A.: Global meta-analysis of nitrogen fertilizer use efficiency in rice, wheat and maize, Agric. Ecosyst. Environ., 338, 108089, https://doi.org/10.1016/j.agee.2022.108089, 2022.